

UNIVERSITÀ DEGLI STUDI DI PADOVA

DIPARTIMENTO DI TECNICA E GESTIONE DEI SISTEMI INDUSTRIALI
CORSO DI LAUREA MAGISTRALE IN INGEGNERIA MECCATRONICA

MASTER THESIS

Wide Range Control and Performance Evaluation of a Single-Axis Compliant Nano-Positioning System

Supervisor: Dr. Paolo Magnone

Co-Supervisors: Dr. Richard Kavanagh [University College Cork]

Dr. Guangbo Hao [University College Cork]

Candidate: Aldo Marchi

1156672-IMC

ACADEMIC YEAR: 2018-19

This page is intentionally left blank.



UCC

Coláiste na hOllscoile Corcaigh, Éire
University College Cork, Ireland

All the experimental work present in this thesis was conducted at the Mechatronics Lab of the Electrical Engineering Building at the University College Cork, Ireland.

The thesis was developed during the ERASMUS project's stay, between January and September 2018.

This page is intentionally left blank.

Table of Contents

ACKNOWLEDGMENTS	1
ABSTRACT	3
1 INTRODUCTION	5
1.1 Robotics	5
1.2 Nano-Positioning Systems	7
1.3 Flexure Based Compliant Mechanisms [CMs]	9
1.3.1 Advantages/Disadvantages of Compliant Mechanisms	10
1.3.2 Design Approaches & Nonlinearities	11
1.4 Robotic System Analyzed	13
1.4.1 Innovative Features and Possible Applications	15
2 HARDWARE and SETUP DESCRIPTION	19
2.1 Mechanical Structure	20
2.1.1 Compliant Basic Parallelogram Mechanism (CBPM)	20
2.1.2 XYZ Compliant Parallel Manipulator (CPM)	21
2.1.3 Base Frame	23
2.2 Actuator	23
2.3 Encoder	25
2.4 Controller Board	27
2.4.1 dSPACE GUI	28

2.5	Servo Amplifier	29
2.6	Power Supply	30
3	SYSTEM MODELING	31
3.1	Harmonic Oscillator	31
3.2	System Nonlinearities	33
3.2.1	Nonlinear Load-Displacement Equations	34
3.2.2	Primary Actuation Force	35
3.2.3	Primary Motion Stiffness	36
3.2.4	Maximal Motion Range	37
3.2.5	XYZ Stage	39
3.2.6	Nonlinear Oscillator: Duffing Oscillator	41
4	LINEAR CONTROL	45
4.1	Linear Control	45
4.1.1	PID Tuning	45
4.1.2	Motion Control Trajectory	47
4.1.3	Force Feedback and Feedforward Control	49
4.1.4	Velocity Estimation	53
5	NONLINEAR CONTROL	59
5.0.1	Feedback Control	59
5.0.2	Feedforward Control	60
5.1	Nonlinear Range Test Results	61
6	DYNAMIC ANALYSIS	69
6.1	Rate Limiter Function Block	72
6.2	Analysis of the Resonances	74
6.3	New Model	76
6.3.1	Bode Plot	78

6.3.2 Dynamic Characterization and Control	
Accomplishments	79
7 ANALYSIS OF CROSS-COUPLING	81
7.1 Four-Beam Compliant Module Actuation Forces	82
7.2 Test Results	85
CONCLUSIONS	89
Future Work	90
A Manipulator Parameter Values	91
B S-Curve Profile Generator	93
C Nonlinear Stiffness Function	95
D Nonlinear Force Function	97
E Datasheets	99
References	107

This page is intentionally left blank.

List of Figures

1.1	Example Serial Robot: Articulated Robot [1].	6
1.2	Example Parallel Robot: Delta Robot [2].	6
1.3	Graphical Representation of Accuracy, Precision and Resolu- tion [3].	8
1.4	Examples of Traditional Rigid-Body Mechanisms [4].	9
1.5	Bow and Arrow System [3].	10
1.6	Example of Compliant Mechanism [4].	10
1.7	Example of Compliant Joints, Lumped and Distributed [3].	12
1.8	Compliant Parallel Robot under Investigation.	14
1.9	Operating principle of an AFM [5].	16
2.1	System Block Diagram.	20
2.2	CBPM Representation [6].	21
2.3	Actual CBPM of the Manipulator.	21
2.4	The fully-symmetrical XYZ Compliant Parallel Manipulator (CMP): (a) XYZ CMP disassembled [7]; (b) beams involved in the degree of freedom (DOF).	22
2.5	XYZ CPM: (a) the three motion axes highlighted, and (b) the motion along the X-axis [8].	22
2.6	The Manipulator (on the left) and the Geometric Representa- tion of the Anti-Vibrational Feet (on the right) [7].	23
2.7	Voice Coil Actuator Representation [9].	24

2.8	Actual Voice Coil Actuator of the Manipulator.	24
2.9	Optical Linear Encoder Representation.	26
2.10	Actual Optical Linear Encoder of the Manipulator.	26
2.11	DS1104: Amplifier and Encoder connections.	28
2.12	Amplifier Method of Operation.	29
2.13	Block Diagram of the Amplifier.	30
3.1	Mass-Spring-Damper System - Harmonic Oscillator [10].	31
3.2	Bode Plot of the Harmonic Model [3.3].	33
3.3	CBPM with actual geometry, loading and displacement indi- cation [11].	34
3.4	Graph of Primary Actuation Force as a function of Primary Displacement.	36
3.5	Graph of Primary Stiffness wrt Primary Displacement.	37
3.6	The fully-symmetrical XYZ Compliant Parallel Manipulator (CMP) (a) XYZ CMP disassembled (b) beams involved in the degree of freedom (DOF) [7].	39
3.7	A beam deformed in an S-shape [3].	40
3.8	Duffing Oscillator Hysteretic Behaviour [12].	41
3.9	Duffing Oscillator Magnitude Graph, $F_0 = 0.3514$ N.	42
3.10	Duffing Oscillator Hysteresis Graph, $F_0 = 201.5$ N.	43
4.1	PID Step Responses (a) Simulated, (b) Tested.	46
4.2	Portion of a Sine Wave used for the S-Curve Profile.	48
4.3	Responses with Rise Time (a) 0.05 s, (b) 0.1 s and (c) 0.15 s.	49
4.4	Simulink Block Diagram used to calculate the velocity (V) and the acceleration (A) references.	50
4.5	Control Simulink Block Diagram.	51
4.6	References Block Diagram.	51
4.7	Newton Block Diagram.	52

4.8 PID Block Diagram.	52
4.9 Feedforward Block Diagram.	53
4.10 System Block Diagram.	53
4.11 Observer Block Diagram (Laplace Domain) [13].	54
4.12 Discrete Observer Block Diagram [13].	55
4.13 Simulation Velocity Plot (Hard).	57
4.14 Simulation Velocity Plot (Medium).	57
4.15 100 nm displacement, velocity estimated by derivative.	57
4.16 100 nm displacement, velocity estimated by observer.	57
4.17 Discrete Observer, Simulink Block Diagram.	58
5.1 Nonlinear Feedback Control Simulink Block Diagram.	60
5.2 Simulink Block Diagram for Nonlinear Feedforward Control.	61
5.3 Positive Displacement Direction.	62
5.4 Pre-Tuning Nonlinear Control, 0.1 mm displacement (Rise Time = 0.1 s).	62
5.5 Pre-Tuning Nonlinear Control, -0.1 mm displacement (Rise Time = 0.1 s).	62
5.6 Pre-Tuning Nonlinear Control, 0.8 mm displacement (Rise Time = 0.1 s).	63
5.7 Pre-Tuning Nonlinear Control, -0.8 mm displacement (Rise Time = 0.1 s).	63
5.8 Pre-Tuning Nonlinear Control, 1 mm displacement (Rise Time = 0.1 s).	63
5.9 Pre-Tuning Nonlinear Control, -1 mm displacement (Rise Time = 0.1 s).	63
5.10 Post-Tuning Nonlinear Control, 0.1 mm displacement (Rise- time = 0.1 s).	64
5.11 Post-Tuning Nonlinear Control, -0.1 mm displacement (Rise- time = 0.1 s).	64

5.12 Post-Tuning Nonlinear Control, 0.8 mm displacement (Rise-	
time = 0.1 s).	65
5.13 Post-Tuning Nonlinear Control, -0.8 mm displacement (Rise-	
time = 0.1 s).	65
5.14 Post-Tuning Nonlinear Control, 1 mm displacement (Rise-	
time = 0.1 s).	65
5.15 Post-Tuning Nonlinear Control, -1 mm displacement (Rise-	
time = 0.1 s).	65
5.16 Pre- and Post- Tuning Comparison of the Force Magnitude	
within 1 mm Range.	68
6.1 Example of a Sinusoidal Waveform with Variable Frequency,	
variation of 1 Hz per s.	69
6.2 Sinusoidal Waveform Reference with Variable Frequency, 0 Hz	
to 300 Hz (1 Hz/s), Amplitude 300 nm.	70
6.3 Sinusoidal Waveform Reference with Variable Frequency, 0 Hz	
to 300 Hz (1 Hz/s), Amplitude 3 μm without end effector and	
tightened connection.	71
6.4 Sinusoidal Waveform Reference with Variable Frequency, 0 Hz	
to 300 Hz (1 Hz/s), Amplitude 10 μm .	72
6.5 Sinusoidal Waveform.	73
6.6 Plot of the frequency limit in function of the displacement,	
where $f = \frac{0.135}{4 \cdot \Delta x}$.	73
6.7 Sinusoidal Waveform Reference with Variable Frequency, 0 Hz	
to 300 Hz (1 Hz/s), Amplitude 3 μm , improved inertia.	75
6.8 Clamped Base Frame.	75
6.9 Response of Clamped System.	75
6.10 Variable Sinusoidal output-input.	76
6.11 PRBS output-input.	76

6.12 Sinusoidal Waveform Reference with Variable Frequency, 0 Hz	
to 300 Hz (1 Hz/s), Amplitude 1 μm , new model (6.4).	77
6.13 Sinusoidal Waveform Reference with Variable Frequency, 0 Hz	
to 300 Hz (1 Hz/s), Amplitude 1 μm , new model with original	
stiffness.	78
6.14 Bode Plot old (6.2) vs new model (6.4).	78
7.1 Cross-Axis Coupling Along the X-axis in a Compliant Mech-	
anism (5).	81
7.2 Four-Beam Compliant Module (5).	82
7.3 3D plot of ΔF_x .	84
7.4 Cross-Axis Coupling Effect, Positive X-Axis Displacement.	86
7.5 Cross-Axis Coupling Effect, Negative X-Axis Displacement.	87

This page is intentionally left blank.

List of Tables

1.1 Applications of XYZ CPMs [5].	17
2.1 VCA LA30-48-000A Parameters Datasheet.	25
2.2 DS1104 Processor and Memory Datasheet.	27
2.3 Specs of the Amplifier.	29
4.1 Ziegler-Nichols' Gains Evaluation Table [14].	46
4.2 PID Gains.	47
4.3 Observer Gain Values.	56
5.1 Error Comparison Between the Pre- and Post- Tuning Force Law.	66
7.1 Cross-Axis Coupling Force Effect Along the X-Axis.	88
A.1 Manipulator Parameter Values.	92

This page is intentionally left blank.

ACKNOWLEDGMENTS

I would like to sincerely thank both my co-supervisors, Dr. Richard Kavanagh and Dr. Guangbo Hao. Dr. Richard Kavanagh always supported me through all the phases of the thesis. Furthermore, I have really appreciated his audit work on my report. Dr. Guangbo Hao introduced and guided me into the world of compliant mechanisms and assisted me in the understanding of the system analyzed. I thank them for their help in both my studies and my stay in Cork.

Last but not least, I would like to thank my primary supervisor, Dr. Paolo Magnone, for correcting my thesis. Because his valuable comments, the thesis has been improved.

This page is intentionally left blank.

ABSTRACT

This thesis is focused on the development of compliant nano-positioning system. A compliant mechanism is a type of mechanism which transfers or transforms motion, force, or energy by the deflection of flexible members. Whereas, a nano-positioning device is a mechanism capable of motion control at the nanoscale.

In the first place, the mechanical design is presented and each component is thoroughly described. The system layout consists of the nanopositioner itself, a controller board, a voice coil actuator, a servo amplifier, an optical linear encoder and a DC power supply. The system can be modeled as an harmonic oscillator in a small range up to 0.2 mm and as a duffing oscillator beyond that range. Both models are analyzed and applied to the system. The control algorithm developed is based on a PID feedback position control and a force feedforward control.

In particular, this thesis focuses on the presentation of three achievements. The first goal has been to improve the closed-loop control with force feedforward in order to reach the desired range of 1 mm while taking into account the nonlinearities of the system. Secondly, the dynamic behaviour of the manipulator, up to 300 Hz, has been analyzed and enhanced by an improved model and setup. Finally, the effect of cross-axis coupling in the actuation force has been examined through a significant number of tests.

This page is intentionally left blank.

Chapter 1

INTRODUCTION

1.1 Robotics

Robotics is an interdisciplinary branch of engineering and science that includes mechanical engineering, electronic engineering, computer science, and others. Robotics deals with the design, construction, operation, and use of robots, as well as computer systems for their control, sensory feedback, and information processing.

A robot is "a reprogrammable, multifunctional manipulator designed to move material, parts, tools, or specialized devices through various programmed motions for the performance of a variety of tasks"

Robot Institute of America, 1979

Mechanically, a robot is formed by a series of elements or links connected by joints that allow a relative movement between each pair of consecutive links; the way in which the links are connected can correspond to either open or closed kinematic chains.

Robots split into two main families: serial robots and parallel robots.

A *Serial Robot* has an open chain, where the base is linked to the end-effector by a series of links connected by moveable joints actuated by different motors and they are the most common manipulators employed in industry. An example of serial robot is shown in Figure [1.1](#).

On the other hand, a *Parallel Robot* has a closed chain, where the end effector is directly connected to its base by a number of separate and independent links working simultaneously. An example of parallel robot is shown in Figure [1.2](#).

Although most of the robots or manipulators that are in use are hinged arms with serial structure, the development of robots with parallel structure is currently of great interest. Among some of the applications of the parallel robots are: flight simulators, manufacturing processes, and some tools for surgery in which high positioning accuracy is needed.

Parallel robots have several advantages compared to Serial robots: they provide greater load capacity, high speed and high-precision positioning.

However, they present some drawbacks, such as the reduced workspace, the difficulty of finding a solution of direct kinematics and the analysis of singular configurations.

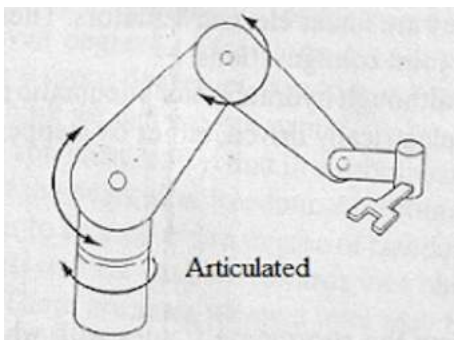


Figure 1.1: Example Serial Robot: Articulated Robot [\[1\]](#).

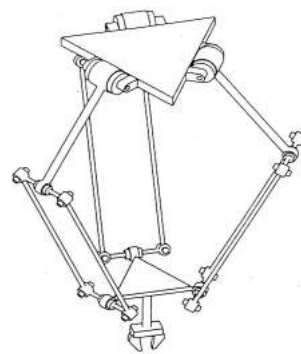


Figure 1.2: Example Parallel Robot: Delta Robot [\[2\]](#).

1.2 Nano-Positioning Systems

Nowadays, the nano-world is no more just a concept, it is a request of lots of new technologies, and everyday more such technologies are being developed. This has been possible thanks to the recent improvements of nano-metrology which has led to the development of the new field of nanotechnology. In the past decade, it has become evident that nanotechnology will make fundamental contributions to science and technology; as a matter of fact, the commercialization of products based on advancements in nanoscale technologies has already began emerging. Inevitably, most schemes of nanotechnology impose severe specifications on positioning. This demand for ultrahigh positioning precision forms a pivotal requirement in many applications of nanotechnology. For instance, nano-positioning systems are important in a variety of optical systems, in life science for data acquisition and processing, in the production development for miniaturization, in microelectronics and so on.

The aforementioned level of precision of movement evidently cannot be achieved by the unaided human hand, hence a device capable of nano motion quality is mandatory. A nanomanipulator is a mechatronic motion system which is able to achieve a motion quality of 100 nm or less.

Such high-precision motion quality is mainly determined in terms of:

- i) *accuracy*, i.e. the closeness of agreement between a test result and the accepted reference value [15].
- ii) *precision*, i.e. the closeness of agreement between independent test results obtained under stipulated conditions [15].
- iii) *resolution*, i.e. the smallest allowable position increment.

These descriptors are depicted in Figure 1.3, which describes them in a more effective way.

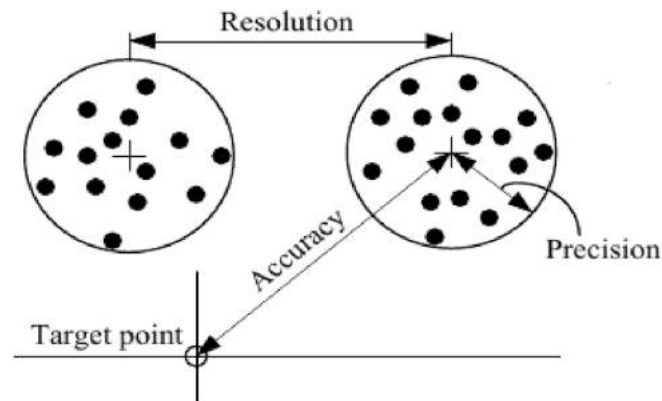


Figure 1.3: Graphical Representation of Accuracy, Precision and Resolution [3].

The motion quality is not the only goal, it is desirable to have a high bandwidth and a wide range as well. The right choice of the components and a proper design of the manipulator become crucial. These manipulators are made up of actuators, drivers, sensors, a flexure bearing and controls implemented on a microcontroller or DSP.

For example, voice coils are the best one for large-range nano-positioning due to hysteresis free, frictionless, cog-free, linear model, and direct control of actuation force. Their resolution is limited by the SINAD (signal to noise and distortion ratio) of the current driver (amplifier), which however, can be improved by the partially customized low-noise hardware and partially feedback control.

Traditional mechanisms suffer from backlash, high wear and friction which make them often inapplicable due to some immediate requirements for lower cost and higher performance; on the other hand, compliant mechanisms become an excellent choice: no backlash, reduced wear and friction, and they can be used in a variety of applications, including both micro and macro scales.

1.3 Flexure Based Compliant Mechanisms [CMs]

A mechanism is a mechanical device used to transfer or transform motion, force, or energy. Traditional rigid-body mechanisms consist of rigid links connected at movable joints; two of them are shown in Figure 1.4 as an example.

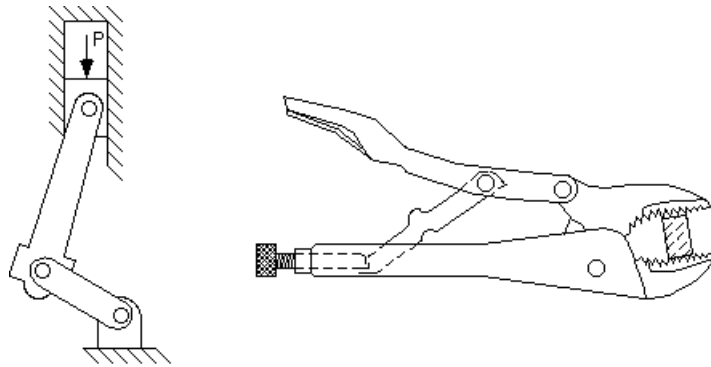


Figure 1.4: Examples of Traditional Rigid-Body Mechanisms [4].

A compliant mechanism also transfers or transforms motion, force, or energy. Rigid-link mechanisms achieve their mobility from movable joints only, whereas, compliant mechanisms use the deflection of their flexible members in order to gain, partially or totally, their mobility. A bow and arrow system is a simple example of this (Figure 1.5). Energy is stored in the limbs as the archer draws the bow. This potential energy is then transformed to kinetic energy of the arrow. Another example of a CM is shown in Figure 1.6. The input force is transferred to the output port, where some energy is stored in the form of strain energy in the flexible members [16].

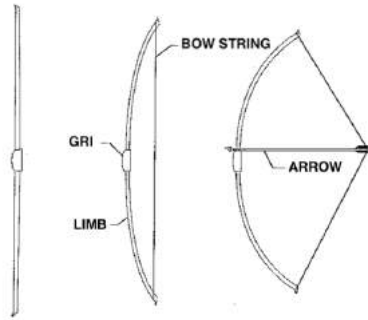


Figure 1.5: Bow and Arrow System [3].

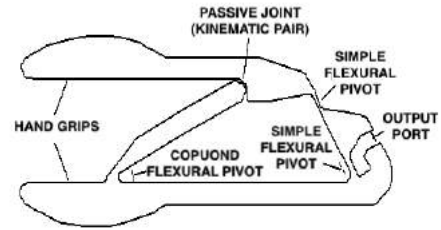


Figure 1.6: Example of Compliant Mechanism [4].

1.3.1 Advantages/Disadvantages of Compliant Mechanisms

A compliant mechanism can be considered the best choice in many applications for several reasons. CMs are usually made up of a smaller number of parts over their rigid-body counterparts to accomplish the same task, which is a great advantage in lots of cases. Furthermore, a lower number of parts often simplify manufacturing and assembly, reducing the production time and costs. These mechanisms are made by precision manufacturing methods which can be contact or noncontact machining which raise the reliability. Contact machining methods include milling machining, while non-contact machining includes laser cutting, water jet and electrical discharging machining.

Compliant mechanisms, unlike traditional ones, can have less movable joints or they can be even jointless reducing wear and need for lubrication. For instance, these characteristics are helpful for applications where the mechanism is not easily accessible, or where its joints can be worn out by operations in harsh environments. The reduction of the number of joints can also increase the mechanism precision, since backlash may be reduced or eliminated. Using a compliant mechanism can lead to a significant reduc-

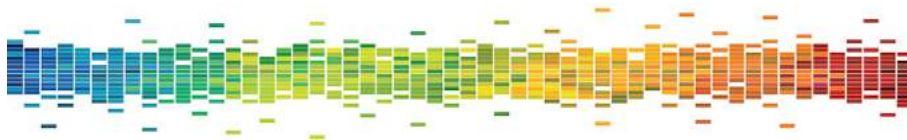
tion in weight when compared with their rigid-body equivalents. This is a fundamental requirement in many applications such as in aerospace and in automotive industry.

Compliant mechanisms can also be easily miniaturized. Indeed, devices as micro structures, actuators, and sensors are widely used, as well as many other microelectromechanical systems (MEMS) which are becoming more and more popular [16].

CMs are also excellent when hygiene is demanded, leading to a lack of contamination in medical application or extreme vacuum environments.

Unfortunately, compliant mechanisms have also several drawbacks. A huge obstacle is the complexity of the design and the analysis of the mechanism. Another one is the motion range, which is limited compared to its non-compliant counterpart, a property that reduces the number of possible applications.

1.3.2 Design Approaches & Nonlinearities



Design and development of compliant mechanism based systems, with precision motion, are becoming critical for the micro-precision industry. Opting for a compliant design can lead to monolithic, jointless, no-assembly devices which are particularly befitting for small range motion applications. CMs can be classified as fully (Fig. 1.7b-c) or partially (Figure 1.7a) compliant, with lumped (Figure 1.7b) or distributed (Figure 1.7a) compliant modules. Lumped-compliant modules having high stiffness, less axial deformation, good dynamics and are easily used to construct systems with minimized deformation effects over motion. However, they have drawbacks such

as small motion range, stress-concentration and complicated modelling. On the other hand, distributed-compliance modules have a larger displacement, less stress-concentration and simpler modelling, but lower stiffness, worse dynamics, large axis deformation and large deformation effect over the motion range.

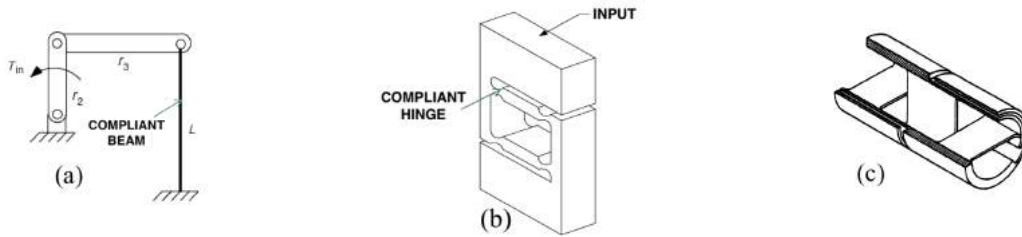


Figure 1.7: Example of Compliant Joints, Lumped and Distributed [3].

The design process is a fundamental part of producing a new product. Shown below the main design approaches [3]:

- *Pseudo-Rigid-Body-Model Approach [PRBMA]*: CMs are obtained by replacing the traditional kinematic joints with suitable lumped-compliance joints based on type synthesis of rigid-body mechanisms.
- *New Kinematics Approach [NKA]*: as just mentioned, the traditional PRBM approach only replaces traditional joints with lumped-compliance joints, while the NKA replaces kinematic chains with appropriate compliant parallel modules as well. Therefore, this new approach fully takes advantage of the potentials of compliance producing better CPMs with more compact configurations.
- *Exact-Constraint-Based Design Approach [E-CBDA]*: the basic idea is that the motion of a rigid-body is determined by the position and orientation of the constraints which provide the essential understanding of kinematics required for the design of real constraint systems. These

constraints can be determined by following the statements that appear in [17].

- *Screw Theory Based Approach [STBA]*: this approach is based on the Screw Theory which enunciates that a generic movement of a rigid body can be described by a rotation around a single axis and by a translation along the same axis; this combined movement is called Screw or Twist. The two fundamental concepts in screw theory are "twist" representing a general helical motion of a rigid body about an instantaneous axis in space and "wrench" representing a system of force and moment acting on a rigid body.

Another issue in the design process is the presence of nonlinearities. Linearized beam equations are valid as long as the deflection of the flexible members is enough small. When the deflection is too large, it is necessary to use nonlinear equations which take into account the geometric nonlinearities of the flexible members. This further obstacle led in the past to design compliant mechanisms by trial and error approaches. Such methods produce, of necessity, very simple systems. Most of the time, these systems are capable to perform only simple tasks, and are not cost efficient for many potential applications. Nonetheless, in recent years theory has been developed to simplify the analysis and design of compliant mechanisms, significantly reducing the previous limitations [16].

1.4 Robotic System Analyzed

The manipulator considered in this thesis is a parallel one with an hybrid structure, designed for purposes which require extremely high precision providing the possibility to work at the nanoscale. In order to achieve such working abilities, the components of the robot are compliant. The robot

is displayed in Figure 1.8 and it will be thoroughly described in the next chapter.



Figure 1.8: Compliant Parallel Robot under Investigation.

The project of the positioner is quite big and complex and it has been carried on by more students:

- *Haiyang Li - PhD Thesis [UCC]:* complete design of the spatial translational compliant parallel mechanism (XYZ Stage). (before 2016)
- *Fabiana Federica Ferro - Master Thesis in Automation Engineering [UNIPD]:* complete setup of the system and closed-loop control in the linear range. (2016)
- *Sandon Riccardo - Master Thesis in Product Innovation Engineering [UNIPD]:* closed-loop control with force feedforward with high motion quality (30 nm) in the linear range, in static conditions.

Project Purpose *The final aim of this project is to develop a 3 DOFs nano-positioning system with a bandwidth up to 1 kHz where each axis (xyz) has a bidirectional range up to 1 mm.*

It is important to notice that the aforementioned mechanism is fully symmetrical, so that the study of a single axis is sufficient to understand the

behaviour of every axis taken on its own. However, there is a minor unwanted coupling effect when two or more axes are working at the same time. The latter was investigated separately.

The first intent of this thesis is to improve the closed-loop control with force feedforward in order to reach the desired range of 1 mm, taking into account the nonlinearities of the system. Subsequently, the dynamic behaviour of the robot is analyzed and enhanced by an improved model and setup. Finally, the cross-axis coupling effect between two axes is experimentally assessed.

The research has been conducted as follows:

- understanding the adopted software, hardware and previous work;
- minor improvement of the close loop control in the linear range;
- insertion of a velocity observer in the feedback of the closed-loop → noise reduction;
- replacement of the drive → in order to have enough power to work in the nonlinear range;
- definition of the mechanical range limit;
- improvement of the control → in order to work in the nonlinear range;
- dynamic tests and understanding of the resonances;
- improvement of the model;
- assessment of the cross coupling effect.

1.4.1 Innovative Features and Possible Applications

The manipulator taken into account in this thesis presents a new XYZ Compliant Parallel Manipulator (CPM) for Micro/Nano-Manipulation. It has been designed by a new design approach which produced a compact and symmetric configuration. It is made up of just wire beams, instead of traditional sheet beams. As a result, the designed XYZ CPM not only provides translations along the three orthogonal directions, but also has desired mo-

tion characteristics such as reduced cross-axis coupling rates and minimised lost motion rates. Thus, the control system design is considerably eased. Moreover, the wire beams require less actuation force than the sheet beams, feature which allows easier enhancement of the bandwidth [8].

There are several possible applications for this kind of manipulator: they are suitable for a wide range of 2D and 3D nano- and micro-manipulation applications such as nano-/micro-assembly, optical component alignment, metrology applications, 3-axis force sensors, microscopy and spectroscopy applications. Some of the applications can be seen from Table 1.1.

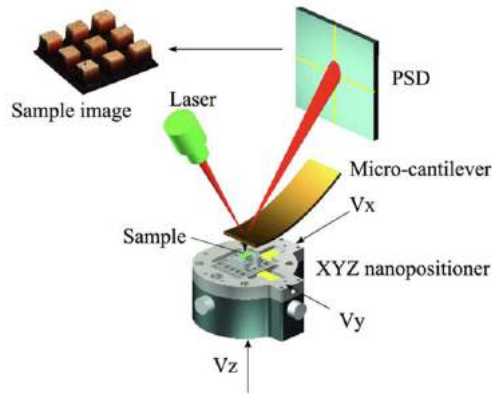


Figure 1.9: Operating principle of an AFM [5].

It is important to note that Atomic-Force Microscopy (AFM) is one of the most successful applications of XYZ CPMs. AFMs are able to gauge and potentially change the mechanical properties of a sample and they are able to create a 3D image of the surface. The one displayed in Figure 1.9 employs a laser and a position-sensitive detector (PSD) to scan the sample [5].

Application Field	Application Description
Micro assembly	Assembly of micro components
Nano-/micro-positioning	High accuracy nanopositioning along X-, Y- and Z-axes
Optics	Handling of small components and assemblies
Optical tweezers and optical traps	Manipulating nano- and micro-meter sized electric particles
Optical fibre alignment	Accurate motion and placement of individual fibres for alignment
Metrology	Accurate measurement of motion and placement
AFM/SPM/MFM/Reflectance	Accurate placement of specimen for examination
Spectroscopy	Measurement of radiation intensity as a function of wavelength
Fluorescence microscopy and spectroscopy	Accurate placement of specimen for examination
Super resolution microscopy	Accurate placement of specimen for examination
Photovoltaics	Component alignment
MEMS	Accurate handling of nano and micro-electronic mechanical systems
Nano-fabrication, Nano-patterning and Nano-machining	Accurate positioning with precision motion is needed to manufacture small, detailed components
Magnetic tweezers, traps and manipulation	Scientific instruments for the manipulation of biomolecules

Table 1.1: Applications of XYZ CPMs [5].

This page is intentionally left blank.

Chapter 2

HARDWARE and SETUP DESCRIPTION

In order to understand the entire research work, it is necessary to take an overview of the nano-positioning system under investigation. Therefore, in this chapter each component of the manipulator is presented and described one by one.

The Compliant Parallel Robot employed is made up of several parts:

- Mechanical Structure;
- Actuator;
- Encoder;
- Controller Board;
- Servo Amplifier;
- Power Supply.

These components will be analyzed separately in the next sections. The general setup of the system can be outlined by the following block diagram

2.1:

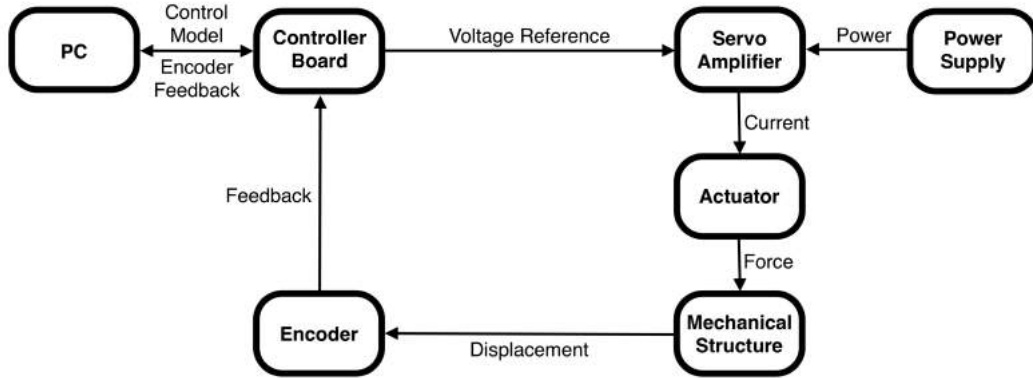


Figure 2.1: System Block Diagram.

2.1 Mechanical Structure

The mechanical structure is fundamentally composed of three parts: a Compliant Basic Parallelogram Mechanism (CBPM), a XYZ Compliant Parallel Manipulator (CPM), and a base frame.

All the components are made by Al 6061-T6 (US) [or 6082-T6 (EU)].

2.1.1 Compliant Basic Parallelogram Mechanism (CBPM)

A compound parallelogram mechanism is composed of two identical parallelogram mechanisms arranged symmetrically and it is a classic example of distributed-compliance translational mechanism. This type of compliant mechanism has been adopted for the implementation of many robotic systems for precision positioning. The CBPM, which consists of two basic parallelogram mechanisms (BPMs), is an example (Figures [2.2](#) & [2.3](#)). This compliant mechanism is an excellent compliant version of the well known traditional P-joint (prismatic-joint), which stands out over the other choices due to its notable characteristics such as non-underconstrained design, alleviated stress concentration, simple symmetrical structure, mitigated buckling, large par-

asitic motion stiffness and avoidance of thermal sensitivity. Nevertheless, its stiffness has a nonlinear behaviour that complicates the analysis and the control design [6].

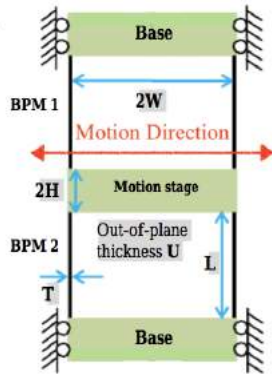


Figure 2.2: CBPM Representation [6].

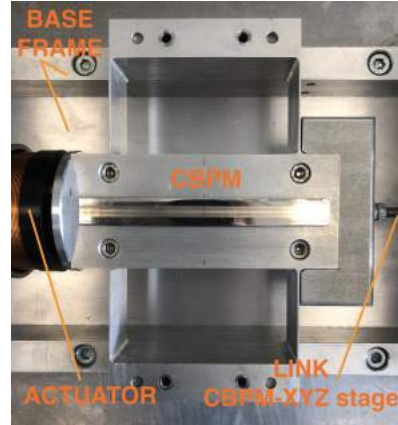


Figure 2.3: Actual CBPM of the Manipulator.

The purpose of the CBPM in our system is dual. On the one hand, it constrains the direction of motion of the voice coil actuator to only the axial direction in order to prevent its damage. On the other hand, it increases the stiffness of the entire mechanism to a suitable value for the size of the actuator.

2.1.2 XYZ Compliant Parallel Manipulator (CPM)

The second member of the positioner involves a fully symmetrical XYZ Compliant Parallel Manipulator (XYZ CPM) described in detail in [8]. As mentioned before in [1.4.1], it has desirable motion characteristics such as reduced cross-axis coupling and minimum lost motion.

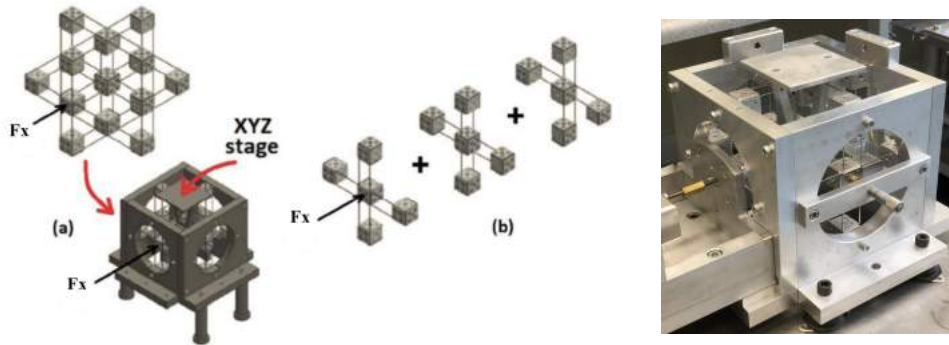


Figure 2.4: The fully-symmetrical XYZ Compliant Parallel Manipulator (CMP): (a) XYZ CMP disassembled [7]; (b) beams involved in the degree of freedom (DOF).

The XYZ CPM has been designed to provide three DOF with completely decoupled motion along the three axes. As a matter of fact, each axis needs its respective actuator and CBPM. However, thanks to the full symmetry of the system, the study of a single axis is sufficient to understand the behaviour of every axis taken on its own. Nonetheless, there is a minor unwanted coupling effect when two or more axis are working at the same time. This effect is debated in Chapter 7.

For instance, the motion along the X-axis is shown in Figure 2.5b.

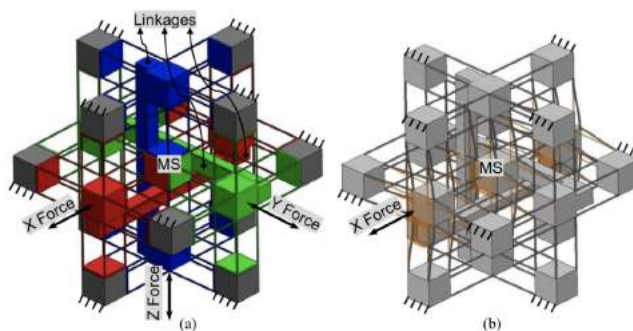


Figure 2.5: XYZ CPM: (a) the three motion axes highlighted, and (b) the motion along the X-axis [8].

2.1.3 Base Frame

The fundamental function of the base frame is to combine all the single parts (the CBPM, the XYZ CPM, the voice coil and the encoder) and, at the same time, to provide a solid structure. Its weight including all the components installed is approximately 25 kg and it is well distributed in 6 legs. Each leg is equipped with suitable anti-vibrational feet [DSD 40 (60 Sh)], in order to improve vibration isolation from the floor [7].



Figure 2.6: The Manipulator (on the left) and the Geometric Representation of the Anti-Vibrational Feet (on the right) [7].

2.2 Actuator

The actuator chosen for the manipulator is the voice coil LA30-48-000A from BEI Technologies INC (Figure 2.8). The voice coil is the best choice for large-range nano-positioning due being hysteresis free, frictionless, cog-free, allowing a linear model and direct control of the actuation force. Voice coils are electric torque motors, namely they do not require a gearbox, and they provide a fast and smooth response. Their resolution is limited by the SINAD (signal to noise and distortion ratio) of the current driver (amplifier), which however, can be improved by the partially customized low-noise hardware and the partially feedback control. Unfortunately, these actuators cannot tolerate transverse forces, which make a device like the CBPM necessary.

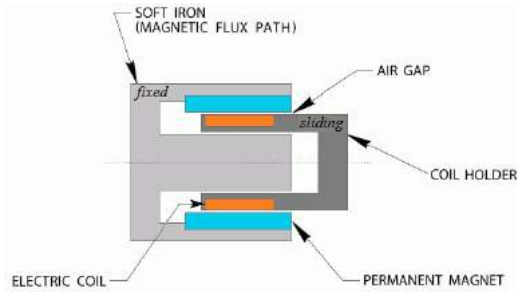


Figure 2.7: Voice Coil Actuator Representation [9].

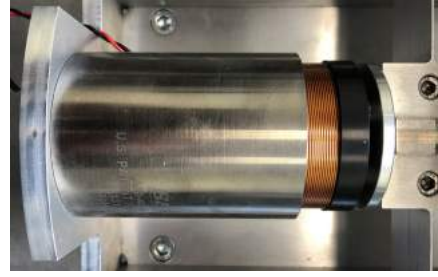


Figure 2.8: Actual Voice Coil Actuator of the Manipulator.

VCA's base their working principle on the Lorentz force. As a matter of fact, they generate their force output by flowing a current through a conductor placed in a magnetic field. The magnetic field is produced by permanent magnets placed on the stator, while the current flows in a coil of wire placed on the rotor. The force generated has a magnitude linearly proportional to the applied current, which is a very convenient feature for the control. In fact, the only variable in the force production which is not constant is the current [9].

The linear law for the actuation force is:

$$F = (k \cdot B \cdot L \cdot N) \cdot i = k_f \cdot i \quad (2.1)$$

where,

k = Force Constant [$\text{N} \cdot \text{m}^{-1}$];

B = Magnetic Flux Density [T];

L = Length of Wire [m];

N = Number of Conductors;

and

k_f = Force Sensitivity (of the Actuator Employed) = $35.14 \text{ N} \cdot \text{A}^{-1}$.

The parameter values of the VCA employed are displayed in Table 2.1.

Linear Actuator Parameters	Units	Symbol	Value
Peak Force	LB	F_P	100
	N		445
Continuos Stall Force	LB	F_{CS}	30.1
	N		133.8
Actuator Constant	LB/ $\sqrt{\text{Watt}}$	K_A	4.9
	N/ $\sqrt{\text{Watt}}$		21.8
Electrical Time Constant	milli-sec	τ_E	1.12
Mechanical Time Constant	milli-sec	τ_M	1.57
Theoretical Acceleration	ft/sec ²	α_T	1962.2
	m/sec ²		598.1
Max Theoretical Frequency @ Full Stroke & Sinusoidal/Triangular Motion	Hz	f_{max}	34.5/38.4
Power I^2R @ F_P	Watts	P_P	419
Stroke:	+ in		0.5
	+ mm		12.7
Clearance on Each side of Coil	in		0.02
	mm		0.51
Thermal Resistance of Coil in still air	°C/Watt	Θ_{TH}	2.3
Maximum Allowable Coil Winding Temp	°C	Temp	155
Weight of Coil Assembly	LB	WT_C	1.64
	G		744
Weight of Field Assembly	LB	WT_T	4.95
	KG		2.25

Table 2.1: VCA LA30-48-000A Parameters Datasheet.

The complete datasheet is shown in Appendix [E](#).

2.3 Encoder

Nano-positioning systems require high resolution encoders. Optical linear encoders dominate the high resolution market because they are the most accurate of the standard styles of encoders, and, as a matter of fact, they currently are the most commonly used in industrial automation applications.

The optical linear encoder used is the SI-HN-4000-01-0-FN-403-003-3 by Renishaw, which provides high speed positional feedback, with 5 nm resolution, and it responds to changes of at most 0.135 m/s (Figures [2.9](#) & [2.10](#)). This resolution limit does not affect the system because the electrical noise

output of the amplifier is higher. As a matter of fact the resolution of the system is 30 nm.

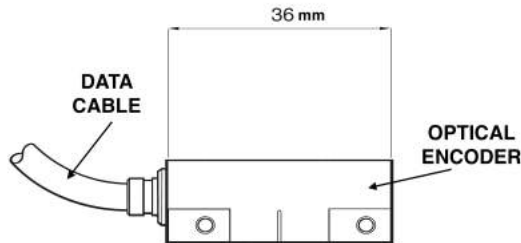


Figure 2.9: Optical Linear Encoder Representation.

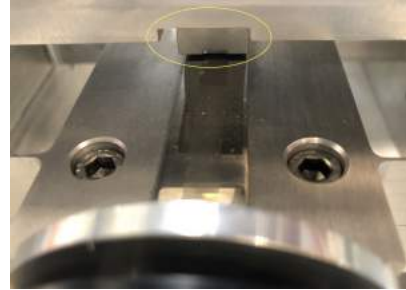


Figure 2.10: Actual Optical Linear Encoder of the Manipulator.

The readhead is fixed on the aluminum frame through a support accurately manufactured and studied directly above the CBPM joint. As previously mentioned, the lost motion of the positioner is negligible thanks to its compliant components, so that one can measure the output displacement on the CBPM joint. The encoder is connected to the controller board and its feedback can be directly accessed from the PC by the controller software using the Signum Serial Interface.

The complete datasheet is shown in Appendix [E](#).

2.4 Controller Board

The DS1104 R&D Controller Board upgrades a PC to a development system for rapid control prototyping.

Parameter		Specification
Processor		<ul style="list-style-type: none"> ■ MPC8240 processor with PPC 603e core and on-chip peripherals ■ 64-bit floating-point processor ■ CPU clock: 250 MHz ■ 2 x 16 KB cache, on-chip.
Memory	Global memory	■ 32 MB SDRAM
	Flash memory	■ 8 MB

Table 2.2: DS1104 Processor and Memory Datasheet.

The controller is connected to the PC through a PCI standard (Peripheral Component Interconnect) which allows the loading of the control program developed and the real-time visualization of all the data related to the board. The program can be developed in Simulink, but it has to be loaded by the dSPACE ControlDesk application if the data is to be displayed.

The dSPACE board is connected to the amplifier and, also to the encoder (Figure 2.11). The DACH1 (Digital to Analog Converter) output connector, with a 16 bit resolution, converts the digital voltage signal coming from the control model to the analogue voltage signal going to the amplifier. It is important to know that the DACH outputs have a maximum output range ± 10 V and a gain of 10 from the value in the Simulink control block. The other side of the encoder is connected to the Digital Incremental Encoder Interface (Inc1).

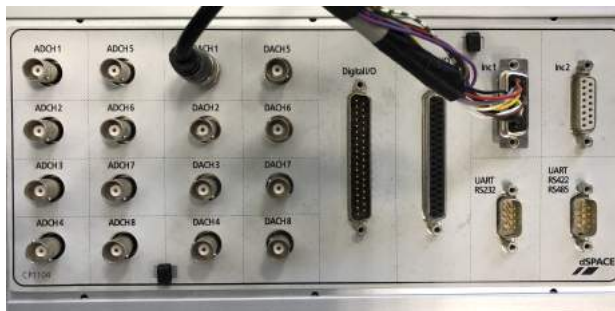


Figure 2.11: DS1104: Amplifier and Encoder connections.

The complete datasheet is shown in Appendix [E](#).

2.4.1 dSPACE GUI

The dSPACE's ControlDesk software represents the PC graphical interface between the DS1104 board and the user. It is a software package with the following modules:

- Experiment management, that allows monitoring of all the data inputs and outputs regarding an experiment;
- Hardware management, that allows the dSPACE hardware configuration and the control of the applications through a graphic interface;
- Instrumentation kits, that offer a great variety of virtual and data acquisition tools.

Furthermore, the program ControlDesk allows monitoring the behaviour of the real-time application variables, making them available to the Matlab Workspace. The user visualize data on the screen, using an oscilloscope or a numerical display, and modify the parameters in real-time. [\[18\]](#)

2.5 Servo Amplifier

The previously-adopted servo amplifier has been changed during this thesis in order to have enough power available to extend the range of operation. The new servo amplifier is the SCA-SS-70-10 by ElectroCraft. It is based on pulse width modulation, PWM four-quadrant PMDC, and its specs are displayed in Table 2.3 and its block diagram in Figure 2.13.

Power Supply Voltage	+11 to +70 VDC (Residual ripple <5 %) (The lower limit is monitored by integrated undervoltage trip) WARNING: Do not exceed 70V. Overvoltage will damage the drive.
Nominal Current	10 A
Peak Current	20 A
Maximum Power (only achievable with additional heatsink & proper mounting, see accessories.)	700 W
Switching Frequency	49 kHz
Efficiency	95 %

Table 2.3: Specs of the Amplifier.

The amplifier is used in the torque mode; in this mode the drive only controls the current in the motor. This control loop is very fast but the speed is load-dependent at constant current. This mode is used in force control applications or as a fast power amplifier for position systems. The current is managed by a voltage reference from the control board. The current (I_{OUT}) is directly related to the voltage reference (V_{IN}) by a constant gain (k_d), see Figure 2.12.



Figure 2.12: Amplifier Method of Operation.

The gain k_d was tuned to provide unity gain ($k_d = 1$). Therefore, the equation [2.1](#) can be rewritten as:

$$F = k_f \cdot i = k_f \cdot (k_d \cdot v) = (k_f \cdot k_d) \cdot v \quad (2.2)$$

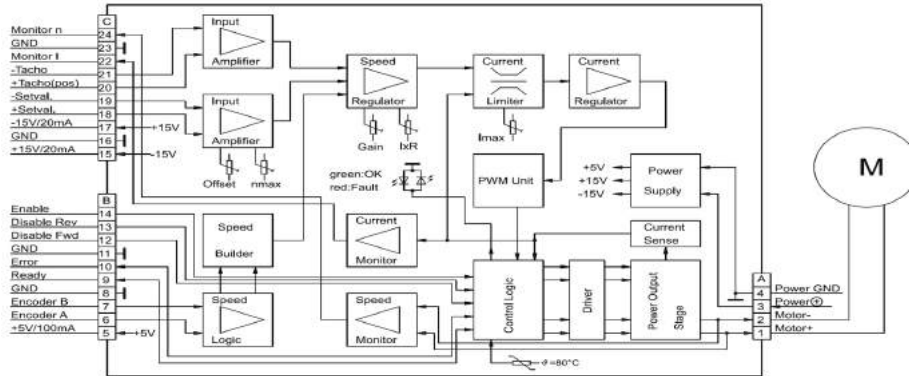


Figure 2.13: Block Diagram of the Amplifier.

2.6 Power Supply

The power supply employed in the system is the SM 52-30 ([V]-[A]) by Delta Elektronika. It is an-high quality DC power supply which provides very stable voltage and current output.



Chapter 3

SYSTEM MODELING

In order to be able to develop the controller of the nanopositioner, it is necessary to study how it can be modelled. Therefore, in this chapter the possible models of the manipulator are presented and analyzed.

The nano-positioning system analyzed can be modeled as an Harmonic Oscillator in its simplest form or, more accurately, as a Duffing Oscillator. These will be studied, focusing mainly on obtaining the Duffing equations of our system.

3.1 Harmonic Oscillator

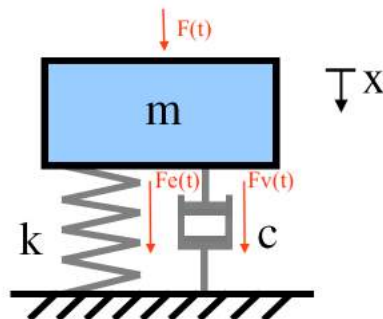


Figure 3.1: Mass-Spring-Damper System - Harmonic Oscillator [10].

Applying Newton's Law to the harmonic oscillator in Figure [3.1](#), one gets:

$$F(t) + F_e(t) + F_v(t) = m \cdot \ddot{x} \quad (3.1)$$

where $F_e = \text{Elastic Force}$ and $F_v = \text{Viscous Force}$. Therefore,

$$F(t) = m_{tot} \cdot \ddot{x}(t) + c \cdot \dot{x}(t) + k_t \cdot x(t) \quad (3.2)$$

where x is the position of the platform, c is the viscous damping coefficient, and k_t is the overall stiffness.

According to [\[19\]](#), the manipulator to be considered has a linear behaviour for displacements smaller than 0.2 mm and it can be modelled as an harmonic oscillator. The values of the nano-positioning system (m_{tot} , c and k_t) are in Appendix [A](#).

The External Force $F(t)$ is the actuation force of the voice coil which corresponds to the formulae [2.1](#) and [2.2](#). Moving the equation [3.2](#) to the laplace domain, one can obtain the transfer function $S(s)$ between the output position $X(s)$ and the input voltage $V(s)$:

$$\begin{aligned} k_f \cdot v(t) &= m_{tot} \cdot \ddot{x}(t) + c \cdot \dot{x}(t) + k_t \cdot x(t) \\ \implies k_f \cdot V(s) &= m_{tot} \cdot s^2 \cdot X(s) + c \cdot s \cdot X(s) + k_t \cdot X(s) \\ \implies S(s) &= \frac{X(s)}{V(s)} = \\ \frac{k_f}{m_{tot} \cdot s^2 + c \cdot s + k_t} &= \frac{35.14}{1.824 \cdot s^2 + 22.353 \cdot s + 129460} \end{aligned} \quad (3.3)$$

where m_{tot} , c and k_t are in Appendix [A](#) and k_f is in Section [2.2](#); all the units of measurement are expressed in the SI, therefore the position x results in metre.

The bode plot of the model [3.3](#) is displayed in Figure [3.2](#). Its natural frequency can be easily evaluated as follows:

$$\omega_n = \sqrt{\frac{k_t}{m_{tot}}} = 266.413 \text{ rad} \cdot \text{s}^{-1} \equiv 42.4 \text{ Hz} \quad (3.4)$$

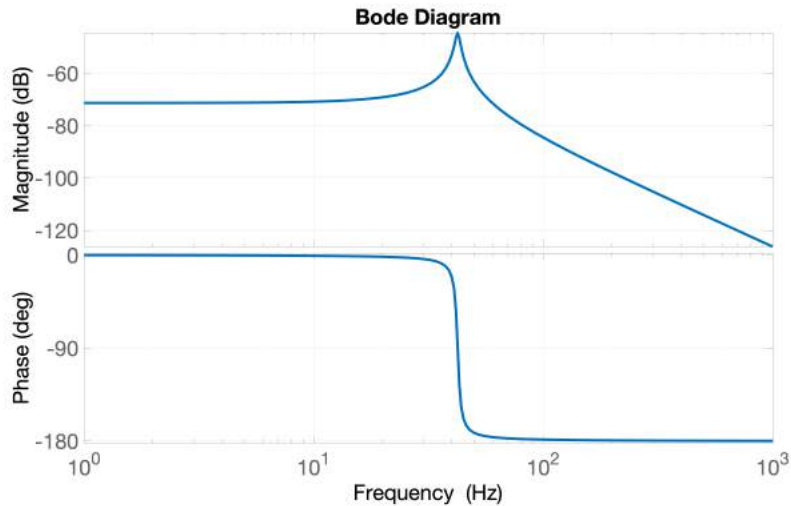


Figure 3.2: Bode Plot of the Harmonic Model [3.3](#).

This model [3.3](#), as mentioned, is valid only in a small range. Therefore, a new model is required that takes into account the nonlinearities of the system, in order to expand the range.

3.2 System Nonlinearities

As discussed in Chapter [2](#), the manipulator is composed by several parts. Nevertheless, the component that is deeply nonlinear is the CBPM. Its stiffness varies over displacement, particularly beyond 0.2 mm. This nonlinearity cannot be neglected because it strongly increases the required actuation force.

In the next sections, the nonlinear force and stiffness equations of the CBPM will be theoretically analyzed.

3.2.1 Nonlinear Load-Displacement Equations

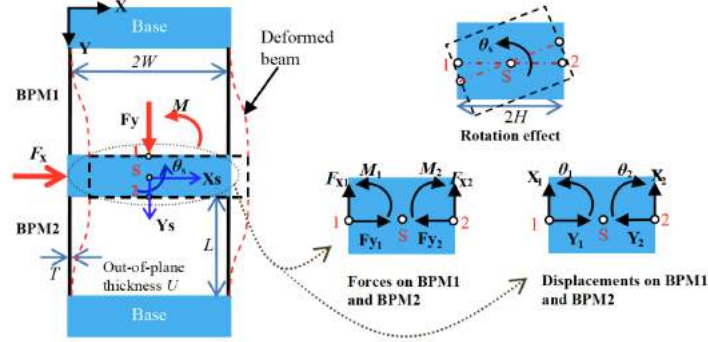


Figure 3.3: CBPM with actual geometry, loading and displacement indication [11].

The specific geometric values for our CBPM (T^1 , U^2 , W^3 , H^4 and L^5) are displayed in Appendix A. F_x and F_y are the actual actuation forces along the two axes, while M is the moment. X_i and Y_i are the actual displacements along the two axes. θ is used to denote the rotations.

A normalization strategy is employed throughout the following derivations, so that all translational displacements and length parameters are normalized by the beam actual length L , forces by $\frac{E \cdot I}{L^2}$, and moments by $\frac{E \cdot I}{L}$ where E is the modulus of elasticity and I is the second moment of area. All the normalized parameters are denoted by the corresponding lower-case letters. On the basis of the definition of the internal forces and displacements for BPM1 and BPM2 in Figure 3.3, the simplified nonlinear load-displacement equations (first-order model) of each BPM for the translations can be represented as [20]:

¹ T is the beam in-plane thickness

² U is the beam out-of-plane thickness

³ W is half of the spanning size

⁴ H is the thickness of the moving stage

⁵ L is the beam actual length

$$\begin{cases} x_i = \frac{f_{x_i}}{24 + 1.2 \cdot f_{y_i}} \\ y_i = (-1)^{i-1} \cdot \left[\frac{f_{y_i}}{2 \cdot d} - 0.6 \cdot x_i^2 + \frac{f_{y_i}}{1400} \cdot x_i^2 \right] \end{cases} \quad (3.5)$$

where $i = 1$ for BPM1 and $i = 2$ for BPM2 and $d = \frac{12}{(T/L)^2}$. The equation [3.5](#) describes how the displacement along the two axes of a simple beam is related to the applied forces.

3.2.2 Primary Actuation Force

The aforementioned normalization strategy is maintained in this section. Considering the rotational effect as indicated in [Figure 2.2](#), the geometrical compatibility conditions for the CBPM can be written as [\[11\]](#):

$$\begin{cases} x_1 = x_S - h \cdot \vartheta_S \approx x_S \\ x_2 = x_S + h \cdot \vartheta_S \approx x_S \\ y_1 = y_S + h \cdot \vartheta_S^2/2 \approx y_S \\ y_2 = -y_S + h \cdot \vartheta_S^2/2 \approx -y_S \\ \vartheta_1 = \vartheta_S \\ \vartheta_2 = -\vartheta_S \end{cases} \quad (3.6)$$

Where simplifications are possible because the translational motion are significantly larger than the parasitic rotation.

In addition, the load-equilibrium equation can be inferred from [Figure 2.2](#):

$$\begin{cases} f_{x_1} + f_{x_2} = f_x \\ f_{y_1} - f_{y_2} = f_y \\ m_1 - m_2 + (f_{x_2} - f_{x_1}) \cdot h + (f_{y_2} - f_{y_1}) \cdot h \cdot \vartheta_S = m \end{cases} \quad (3.7)$$

Combining equations [3.6](#), [3.7](#) and [3.5](#), the following expression for the

primary actuation force can be obtained:

$$f_x = 48 \cdot x_S + \frac{2.88}{\frac{1}{d} + \frac{x_S^2}{700}} \cdot x_S^3 \quad (3.8)$$

3.2.3 Primary Motion Stiffness

Considering the actual, rather than normalized terms, equation 3.8 can be written as:

$$\begin{aligned} \frac{F_x}{\left(\frac{E \cdot I}{L^2}\right)} &= 48 \cdot \frac{X_S}{L} + \frac{2.88}{\frac{1}{d} + \frac{\left(\frac{X_S}{L}\right)^2}{700}} \cdot \left(\frac{X_S}{L}\right)^3 \\ \Rightarrow F_x &= \frac{48 \cdot E \cdot I}{L^3} \cdot X_S + \frac{2.88 \cdot E \cdot I}{\frac{L^5}{d} + \frac{L^3}{700} \cdot X_S^2} \cdot X_S^3 \end{aligned} \quad (3.9)$$

Using the values in Appendix A, the force equation can be plotted as in Figure 3.4

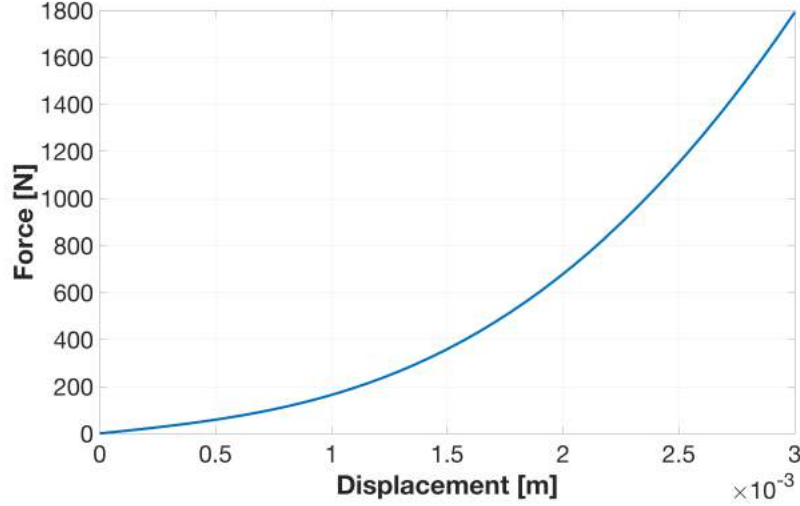


Figure 3.4: Graph of Primary Actuation Force as a function of Primary Displacement.

The equation for the primary motion stiffness can now be obtained as:

$$K_x = \frac{dF_x}{dX_S} =$$

$$\frac{48 \cdot E \cdot I}{L^3} + \frac{8.64 \cdot E \cdot I \cdot X_S^2 \cdot \left(\frac{L^5}{d} + \frac{L^3}{700} \cdot X_S^2 \right) - 5.76 \cdot E \cdot I \cdot X_S^3 \cdot \left(\frac{L^3}{700} \cdot X_S \right)}{\left(\frac{L^5}{d} + \frac{L^3}{700} \cdot X_S^2 \right)^2}$$

$$K_x = \frac{48 \cdot E \cdot I}{L^3} + \frac{8.64 \cdot E \cdot I \cdot X_S^2}{\frac{L^5}{d} + \frac{L^3}{700} \cdot X_S^2} - \frac{5.76 \cdot E \cdot I \cdot L^3 \cdot X_S^4}{700 \cdot \left(\frac{L^5}{d} + \frac{L^3}{700} \cdot X_S^2 \right)^2} \quad (3.10)$$

As reported above, the stiffness equation can be plotted using the values in Appendix A (Figure 3.5)

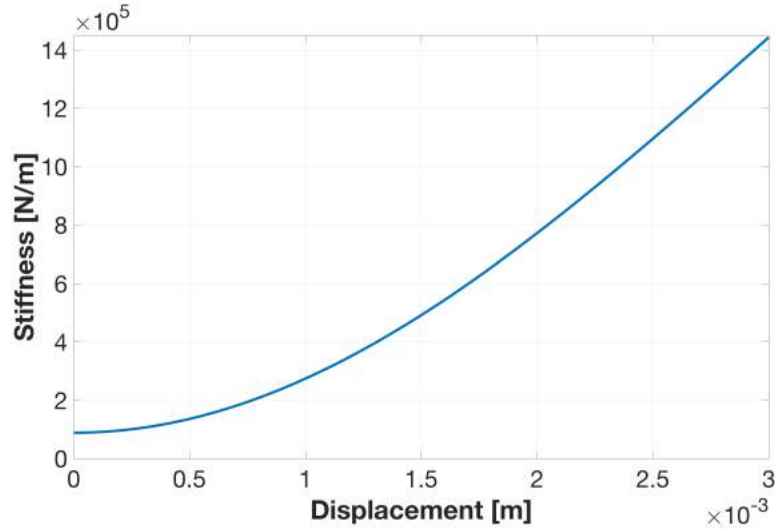


Figure 3.5: Graph of Primary Stiffness wrt Primary Displacement.

3.2.4 Maximal Motion Range

From equation 3.5:

$$f_{y_b} = \frac{f_{y_i}}{2} = \frac{0.6 \cdot x_s^2}{\frac{1}{d} + \frac{x_s^2}{700}} \quad (3.11)$$

From equation 3.11, one can derive the following normalized formula for the end moment for each clamped beam in the CBPM:

$$m_b = (-6 - 0.1 \cdot f_{y_b}) \cdot x_s = -6 \cdot x_s - \frac{0.06 \cdot x_s^3}{\frac{1}{d} + \frac{x_s^2}{700}} \quad (3.12)$$

Neglecting the shear stress effect in the slender beams, the maximal normal stress should meet the following condition to avoid yield:

$$\sigma_{max} = \sigma_B + \sigma_E < \sigma_S \text{ (yield strength)} \quad (3.13)$$

where

$$\sigma_B = \left| \frac{m_b \cdot \frac{E \cdot I}{L}}{\frac{I}{T/2}} \right| = \left| \left(6 \cdot x_S + \frac{0.06 \cdot x_S^3}{\frac{1}{d} + \frac{x_S^2}{700}} \right) \cdot \frac{E \cdot T}{2 \cdot L} \right| \text{ for bending stress}$$

$$\sigma_E = \left| \frac{f_{yb} \cdot \frac{E \cdot I}{L^2}}{A} \right| = \frac{0.6 \cdot x_S^2}{\frac{1}{d} + \frac{x_S^2}{700}} \cdot \frac{E \cdot I}{A \cdot L^2} \text{ for elastic stress (} p_{in} = 0 \text{)}$$

Therefore, σ_{max} in actual terms is:

$$\sigma_{max} = \left| \left(6 \cdot \frac{X_S}{L} + \frac{0.06 \cdot \left(\frac{X_S}{L} \right)^3}{\frac{1}{d} + \frac{1}{700} \cdot \left(\frac{X_S}{L} \right)^2} \right) \cdot \frac{E \cdot T}{2 \cdot L} \right| + \frac{0.6 \cdot \left(\frac{X_S}{L} \right)^2}{\frac{1}{d} + \frac{1}{700} \cdot \left(\frac{X_S}{L} \right)^2} \cdot \frac{E \cdot I}{A \cdot L^2} < \sigma_S \quad (3.14)$$

The material is Aluminum 6061-T6 (US) [or 6082-T6 (EU)], therefore:

- i Tensile Yield Strength $\sigma_S = 276$ MPa
- ii Modulus of Elasticity $E = 69$ GPa
- iii Second Moment of Area (beam) $I = \frac{U \cdot T^3}{12}$

Using the bisection method, the maximum X_S results 3.1353035 mm; it is easy to see in equation [3.14](#) that the result does not change whether X_S is positive or negative.

Applying a safety coefficient of 30%, the range results $X_S \in [-2.2, 2.2]$ mm.

3.2.5 XYZ Stage

The complete compliant mechanism includes an XYZ stage in series with the CBPM, as reported in Figure 3.6. This mechanism gives an extra stiffness constant contribution.

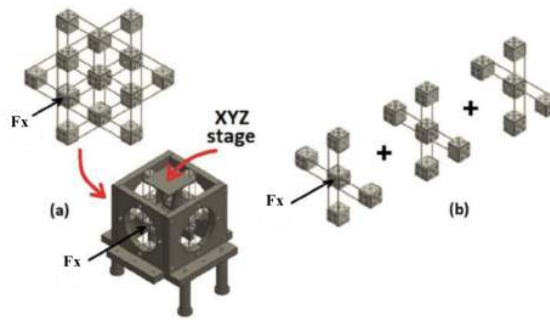


Figure 3.6: The fully-symmetrical XYZ Compliant Parallel Manipulator (CMP) (a) XYZ CMP disassembled (b) beams involved in the degree of freedom (DOF) [7].

Under the assumption of small deflections, we can evaluate this stiffness by the simplified Euler-Bernoulli beam equation:

$$\frac{M(y)}{E \cdot I} = \frac{d\vartheta}{dy} = \frac{d\left(\frac{dx}{dy}\right)}{dy} \quad (3.15)$$

where E is the modulus of elasticity, and I is the second moment of area.

The deformation of one beam of the mechanism XYZ above is illustrated in Figure 3.7:

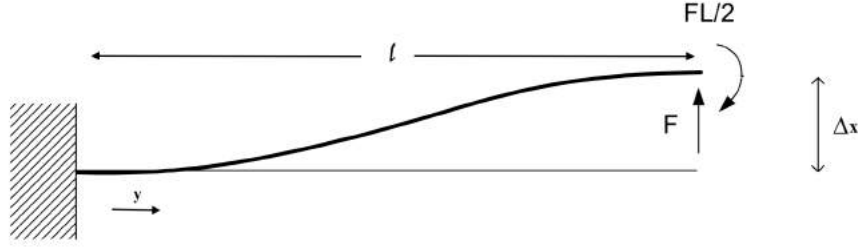


Figure 3.7: A beam deformed in an S-shape [3].

$M(y)$ can be easily evaluated from Figure 3.7 as:

$$M(y) = F(\ell - y) - F \cdot \frac{\ell}{2} = F \cdot \left(\frac{\ell}{2} - y \right) \quad (3.16)$$

Therefore,

$$\delta_x = \iint \frac{F \cdot \left(\frac{\ell}{2} - y \right)}{E \cdot I} \cdot dy \cdot dy = \int_0^{\ell} \frac{F \cdot \left(\frac{\ell}{2} \cdot y - \frac{y^2}{2} \right)}{E \cdot I} \cdot dy = \frac{F \cdot \ell^3}{12 \cdot E \cdot I}$$

$$\Rightarrow k_{single\ beam} = \frac{F}{\delta_x} = 12 \cdot \frac{E \cdot I_{XYZ}}{\ell_{XYZ}^3} = \frac{E \cdot U_{XYZ} \cdot T_{XYZ}^3}{\ell_{XYZ}^3}$$

$$\Rightarrow k_{XYZ} = 24 \cdot k_{single\ beam} = 13248 \frac{N}{m} \quad (3.17)$$

Thus, the equations 3.9 & 3.10 have to be corrected as follows:

$$\bullet \quad F_x = \left(\frac{48 \cdot E \cdot I}{L^3} + k_{XYZ} \right) \cdot X_S + \frac{2.88 \cdot E \cdot I}{\frac{L^5}{d} + \frac{L^3}{700} \cdot X_S^2} \cdot X_S^3 \quad (3.18)$$

$$\bullet \quad K_x = \frac{48 \cdot E \cdot I}{L^3} + k_{XYZ} + \frac{8.64 \cdot E \cdot I \cdot X_S^2}{\frac{L^5}{d} + \frac{L^3}{700} \cdot X_S^2} - \frac{5.76 \cdot E \cdot I \cdot L^3 \cdot X_S^4}{700 \cdot \left(\frac{L^5}{d} + \frac{L^3}{700} \cdot X_S^2 \right)^2} \quad (3.19)$$

3.2.6 Nonlinear Oscillator: Duffing Oscillator

The Duffing oscillator is described by equation [12]:

$$\ddot{x} + \zeta \cdot \dot{x} + \alpha \cdot x + \beta \cdot x^3 = \gamma \cdot \cos(\omega t) \quad (3.20)$$

It is one of the simplest nonlinear systems that, under certain conditions, exhibits chaotic behaviour. Chaos is a characteristic present in a lot of nonlinear systems. Interestingly, chaotic systems have many solutions which are sensitive to initial conditions. That means that even infinitesimally close starting points can diverge to completely different trajectories. Indeed, the frequency response of the Duffing system doesn't follow exactly the expected trajectory. This resonance phenomenon is a sort of frequency hysteresis behaviour, as shown in Figure 3.8.

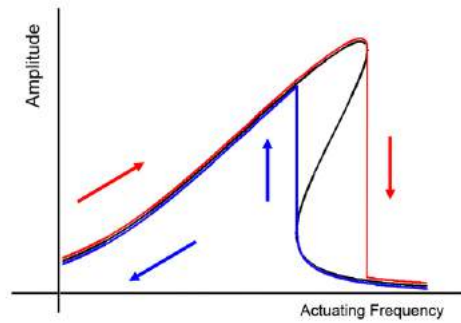


Figure 3.8: Duffing Oscillator Hysteretic Behaviour [12].

The system under investigation is a Duffing Oscillator, and it can be seen from equation [3.9]. In order to examine the response to a periodic forcing (force amplitude $F_0 = k_f \cdot Voltage$), it is useful to rename the parameters and rewrite the Duffing equation as in equation [3.20]:

$$F = m_{tot} \cdot \ddot{x} + c \cdot \dot{x} + \left(\frac{48 \cdot E \cdot I}{L^3} + k_{XYZ} + error L_{av} \right) \cdot x + \frac{error N_{av} \cdot E \cdot I}{\frac{L^5}{d} + \frac{L^3}{700} \cdot x^2} \cdot x^3$$

$$\implies \ddot{x} + \zeta \cdot \dot{x} + \alpha \cdot x + \beta \cdot x^3 = \gamma' \cdot F \quad (3.21)$$

where

$$\zeta = \frac{c}{m_{tot}}; \quad \alpha = \frac{\left(\frac{48 \cdot E \cdot I}{L^3} + k_{XYZ} + error L_{av} \right)}{m_{tot}}; \quad \beta = \frac{\frac{error N_{av} \cdot E \cdot I}{\frac{L^5}{d} + \frac{L^3}{700} \cdot x^2}}{m_{tot}}; \quad \gamma' = \frac{1}{m_{tot}}$$

assuming a harmonic response $x = A \cdot \cos(\omega t + \varphi)$, substituting this in equation [3.20](#) and balancing the first harmonic, one gets [21](#):

$$\gamma^2 = \left[\left(\omega^2 - \alpha - \frac{3}{4} \cdot \beta \cdot A^2 \right)^2 + (\zeta \cdot \omega)^2 \right]^2 \cdot A^2 \quad (3.22)$$

where $\gamma = F_0 * \gamma'$ and A is the amplitude.

In order to plot the magnitude A of our Duffing oscillator, β can be considered as a constant since $\frac{L^3}{700} \cdot x^2$ is negligible.

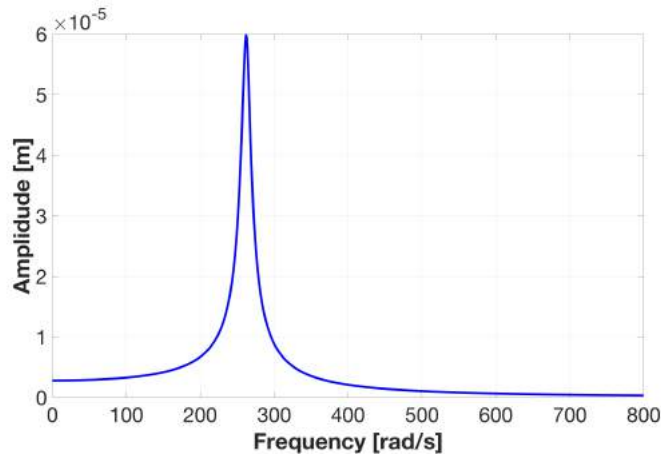


Figure 3.9: Duffing Oscillator Magnitude Graph, $F_0 = 0.3514$ N.

As can be seen from Figure [3.9](#), the chart does not show an hysteric behaviour for a low *Voltage* = 0.01 V ($\implies F_0 = 0.3514$ N) and the resonance is at $\omega = 262.3 \text{ rad} \cdot \text{s}^{-1}$ which is very close to the resonance of the harmonic oscillator model [19](#).

However, if the *Voltage* is increased to 5.7 V ($\implies F_0 = 201.5$ N), the system enters the nonlinear range where the hysteric behaviour of the system is observed.

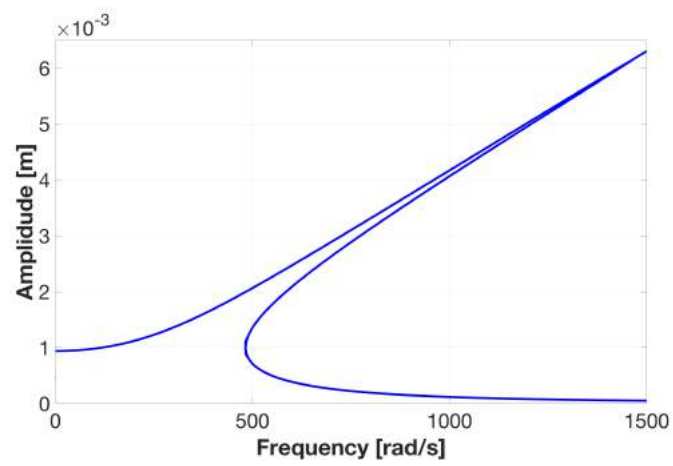


Figure 3.10: Duffing Oscillator Hysteresis Graph, $F_0 = 201.5$ N.

This page is intentionally left blank.

Chapter 4

LINEAR CONTROL

The control algorithm designed for the compliant manipulator is based on two main elements: closed-loop control with position and velocity feedback, and feed-forward control.

In this chapter the control algorithm for the linear range and the related experimental tests will be described.

The main contributions in the linear control performed during the thesis work are:

- i retuning of the PID controller.
- ii selection of the motion trajectory.
- iii addition of velocity feedback control based on a velocity observer.

4.1 Linear Control

4.1.1 PID Tuning

A Proportional–Integral–Derivative (PID) controller has been selected as a control loop feedback mechanism. It is widely used in industrial control applications, thanks to its intrinsic simplicity in both structure and tuning process.

The PID controller of the nano-positioning system has been tuned by the Ziegler-Nichols method. This method is a heuristic method which is performed by setting the integral and derivative gains to zero ($k_i = k_D = 0$). The proportional gain (k_p) is then increased (from zero) until it reaches the maximum gain, k_u , at which the output of the control loop has stable and consistent oscillations with a step variation. The gain k_u and the oscillation period T_u are used to set the k_p , k_i and k_D gains depending on the type of controller used. Voice coils are extremely sensitive and therefore they do not allow high PID gains. The Ziegler-Nichols heuristic method table, adopted in this work, is reported in Table 4.1:

Ziegler-Nichols method			
Control type	Kp	Ti	Td
PI	0.45 K_u	$T_u/1.2$	-
Classic PID	0.6 K_u	$T_u/2$	$T_u/8$
Pressen Integral rule	0.7 K_u	$T_u/2.5$	$3T_u/20$
PID no overshoot	0.2 K_u	$T_u/2$	$T_u/3$

Table 4.1: Ziegler-Nichols' Gains Evaluation Table [14].

The simulation of the linear model [3.3] gave the results, reported in Table 4.2, for the PID controller and the response of the control to a step input gave the results reported in Figure 4.1.

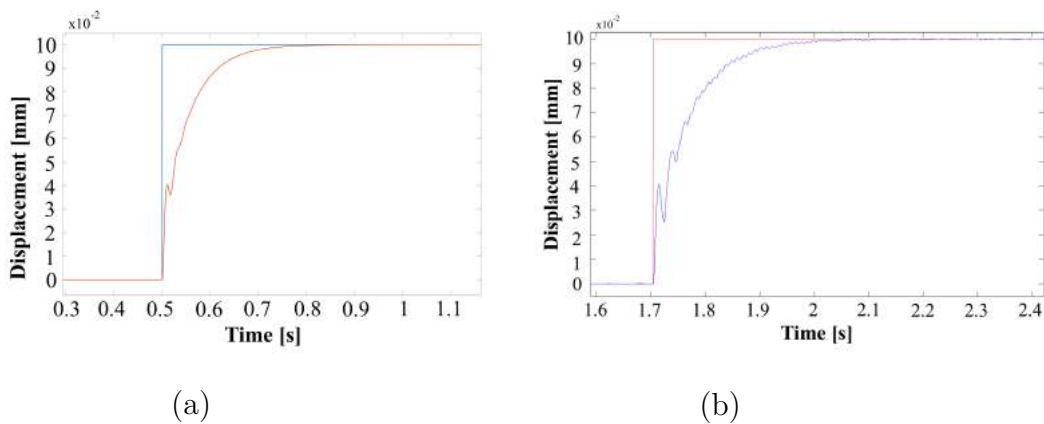


Figure 4.1: PID Step Responses (a) Simulated, (b) Tested.

Parameter	Symbol	Value	Unit of Measurement
Ultimate Gain	k_u	1.0639	-
Oscillation Period	T_u	0.023	s
Proportional Gain	k_p	0.213	-
Integral Gain	k_i	18.5	-
Derivative Gain	k_d	0.0016	-

Table 4.2: PID Gains.

4.1.2 Motion Control Trajectory

A key aspect of control theory is the motion control. It has a wide range of applications in industry, such as manufacturing, targeting, robotics, etc. In motion control systems, closed loop and feedforward regulators are used to control the velocity and position of machines, in order to generate desired motions. The challenge in motion control is always how to achieve precise motion with minimized vibration, and overshoot in position as well as velocity. In the attempt to solve the challenge, trajectory planning has been extensively researched for a few decades. Mechanically feasible and smooth paths with optimized time and minimized overshoots, are always the goals of path planning.

Positioning step variation are not realistic because it requires infinite velocity, as well as all the other derivatives. Additionally, sudden velocity changes tend to cause overshoots, and excite residual vibrations that require time for the machine to reach the final position with the desired precision [22].

For these reasons, different profiles such as s-curve position profiles have been proposed to reduce the tendency to excite system vibration, Figure 4.2.

The s-curve employed as position reference in the nanopositioning system

is the harmonic motion profile defined by the equation [4.1](#).

$$c \cdot \frac{1 - \cos(2\pi f \cdot t)}{2} \quad (4.1)$$

$$\text{defining } c = \frac{2 \cdot s_{des}}{1 - \cos(2\pi f \cdot t_{des})} \text{ and } f = \frac{1}{2 \cdot t_{des}}$$

where s_{des} is the desired amplitude and t_{des} is the desired rise time.

It is the section between two opposite consecutive peaks of a sine wave shifted up of 1 and normalized to 1. Its main property is the null tangent at the beginning and at the end of the rise which follows more realistically the physical behaviour of a system. Therefore, the response is smother and well controlled. The matlab source code used to generate it is in [Appendix B](#).

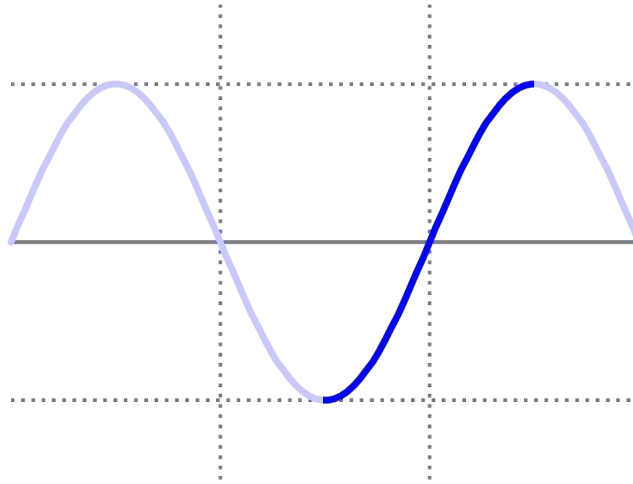


Figure 4.2: Portion of a Sine Wave used for the S-Curve Profile.

It was observed that 0.1 s as rise time was a good trade-off between limited overshoot and fast response time that is evident in [Figure 4.3](#). Hence, only this time value was thenceforth used during the testing.

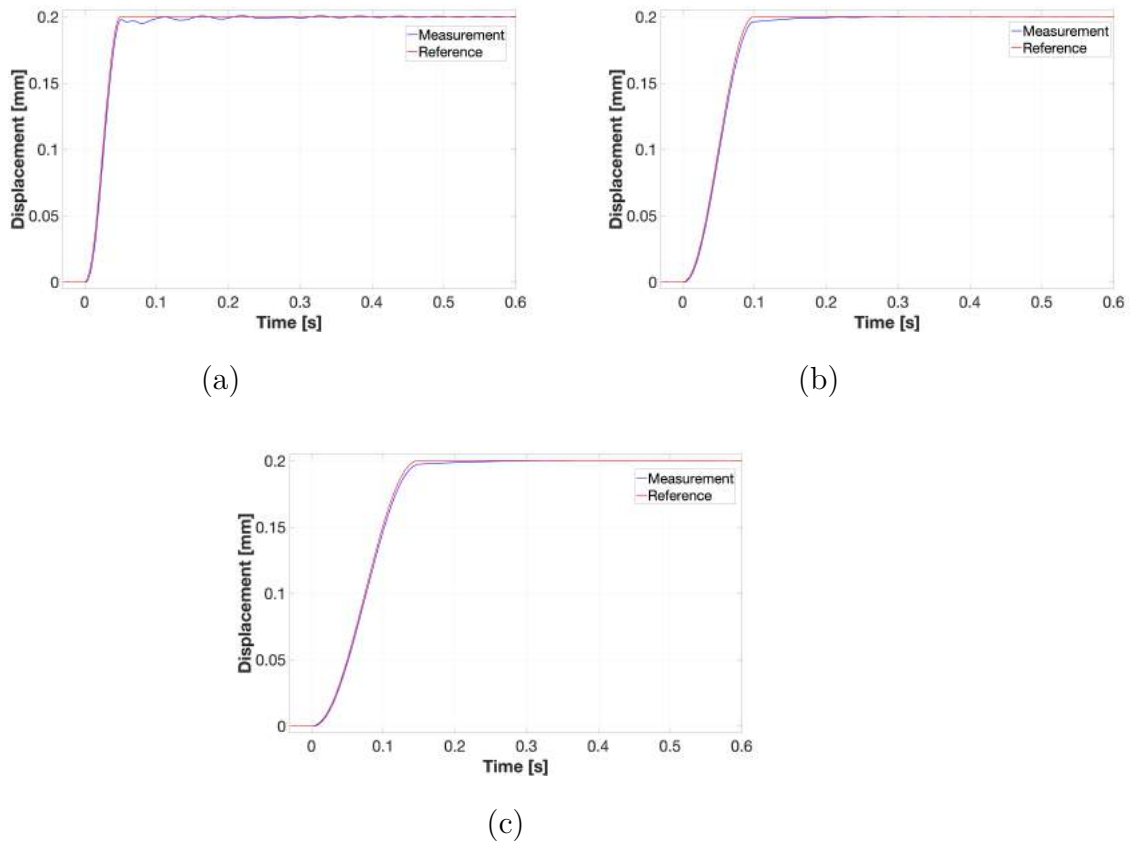


Figure 4.3: Responses with Rise Time (a) 0.05 s, (b) 0.1 s and (c) 0.15 s.

4.1.3 Force Feedback and Feedforward Control

Robert D. Lorenz presents in his paper [23] a state variable approach to force control. He discusses the design techniques required for a manipulator to achieve high-performance force control. He essentially outlines a feedback and a feedforward based control, based on the mass-spring-damper system force model.

In the feedback control, there are two closed-loops: one for the position error, and one for the velocity error. In the manipulators under investigation, the position feedback comes from the linear optical encoder, while the velocity feedback is estimated from the position.

In the feedforward control, the 'best guess' force feedforward is evaluated

by the references of the position, velocity and acceleration according to equation 3.2. The velocity and the acceleration references are calculated by the Simulink block diagram reported in Figure 4.4, where X is the sampled data of the motion profile defined in Section 4.1.2, T_s is the sample time and K is the gain.

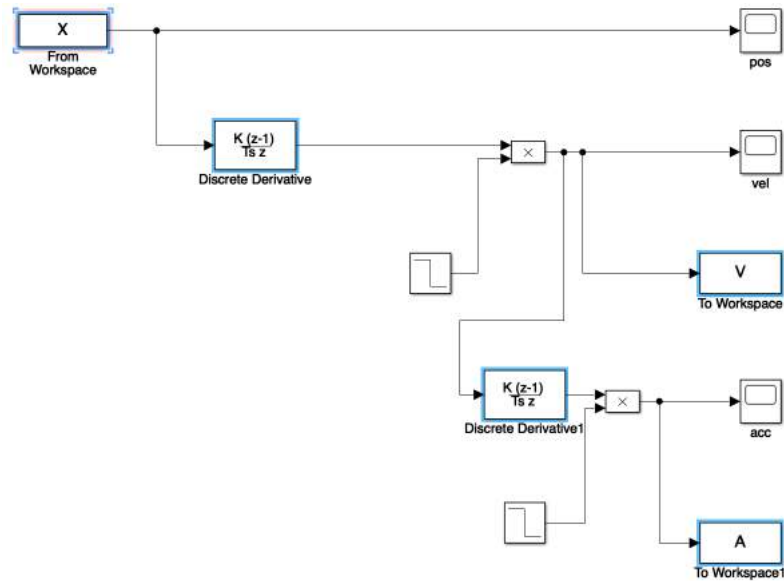


Figure 4.4: Simulink Block Diagram used to calculate the velocity (V) and the acceleration (A) references.

By running a Simulink simulation, it is possible to obtain the derivatives of the position reference. The two step simulink blocks in Figure 4.4 are used to ensure a zero reference value as last sample for the velocity (and acceleration when needed). Finally, the obtained control block diagram is displayed in Figure 4.5.

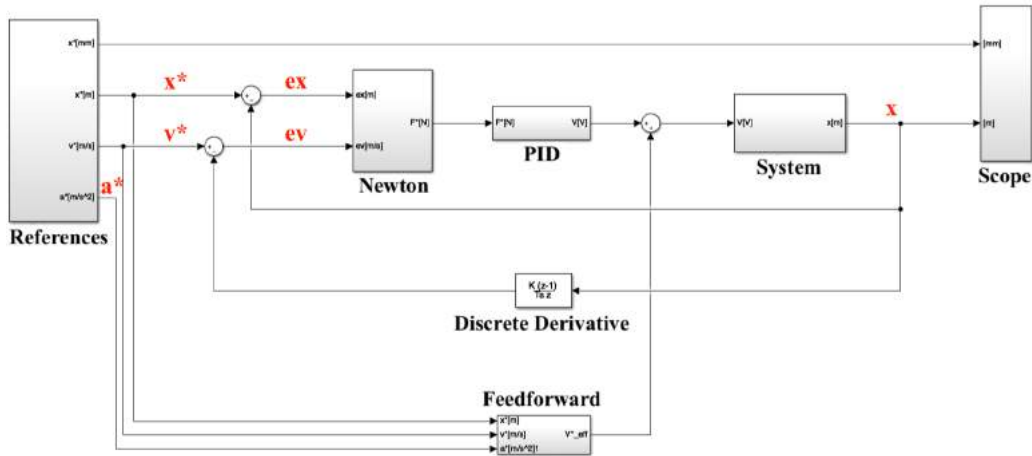


Figure 4.5: Control Simulink Block Diagram.

All the blocks that can be seen in Figure 4.5 will be briefly described below.

- **References** The references in Figure 4.6 are vectors of values from the workspace, normalized to one and properly scaled by the gains. The last value of the workspace vectors (X, V, A) is kept indefinitely.

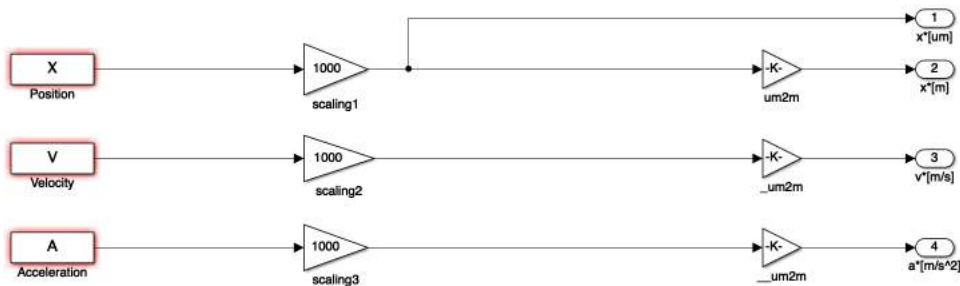


Figure 4.6: References Block Diagram.

- **Newton**

The force required to correct the error is evaluated and used in the feedback control as in Figure 4.7. The gain values come from the linear model 3.3.

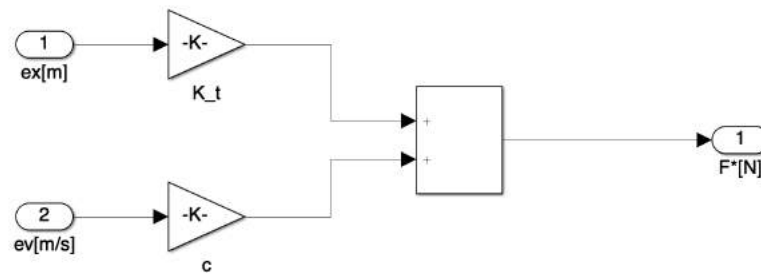


Figure 4.7: Newton Block Diagram.

- **PID**

The PID controller has already been described in Section 4.1.1 and is reported in Figure 4.8.

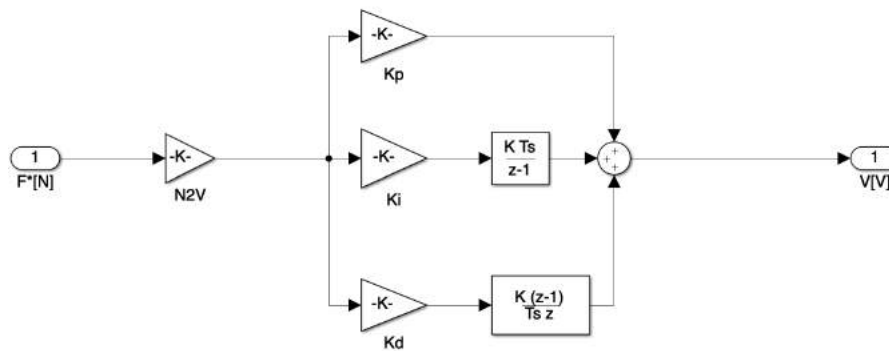


Figure 4.8: PID Block Diagram.

- **Feedforward**

The force best guess is evaluated according to the linear model 3.3 from the references as in Figure 4.9.

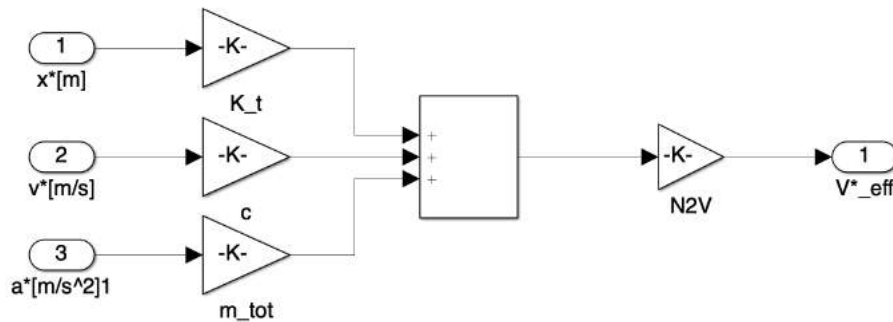


Figure 4.9: Feedforward Block Diagram.

- **System**

The system is the transfer function [3.3](#) in simulation mode, or, as in [Figure 4.10](#), the DAC port in input and the encoder in output (configuration details available in [\[18\]](#)).



Figure 4.10: System Block Diagram.

4.1.4 Velocity Estimation

In order to reduce the noise in the velocity feedback, the derivative of the position feedback has been replaced with a system observer that provides a cleaner velocity feedback for the closed-loop.

Velocity Observer - Continuous Time Analysis

The plant model of a velocity observer in Laplace domain is shown in [Figure 4.11](#)

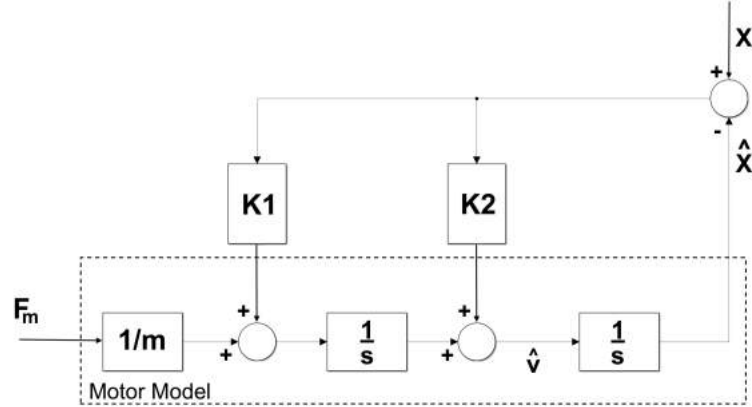


Figure 4.11: Observer Block Diagram (Laplace Domain) [13].

Neglecting for the moment the feedforward input (F_m in Figure 4.11), and using the Laplace domain for simplicity as above, one can derive the equation for K_1 and K_2 [24] (using " $\hat{}$ " to denote the estimation):

$$\begin{aligned}\hat{x} &= \frac{1}{s} \cdot \left[\frac{1}{s} \cdot K_1 \cdot (x - \hat{x}) + K_2 \cdot (x - \hat{x}) \right] \\ \implies \hat{x} + \frac{1}{s^2} \cdot K_1 \cdot \hat{x} + \frac{1}{s} \cdot K_2 \cdot \hat{x} &= \frac{1}{s^2} \cdot K_1 \cdot x + \frac{1}{s} \cdot K_2 \cdot x \\ \implies \hat{x} &= \frac{K_1 + K_2 \cdot s}{s^2 + K_2 \cdot s + K_1} \cdot x\end{aligned}\quad (4.2)$$

Therefore,

$$K_1 = \omega_0^2 \text{ and } K_2 = 2 \cdot \rho \cdot \omega_0 \quad (4.3)$$

where ω_0 is the natural frequency and ρ is the damping factor.

The purpose of the feedforward term is to reduce the position transient error, as is shown below [24]:

$$\begin{aligned}\hat{x} &= \frac{1}{s} \cdot \left[\frac{1}{s} \cdot \left(K_1 \cdot (x - \hat{x}) + \frac{\hat{F}}{m_{tot}} \right) + K_2 \cdot (x - \hat{x}) \right] \\ \implies \hat{x} + \frac{1}{s^2} \cdot K_1 \cdot \hat{x} + \frac{1}{s} \cdot K_2 \cdot \hat{x} &= \frac{1}{s^2} \cdot K_1 \cdot x + \frac{1}{s} \cdot K_2 \cdot x + \frac{1}{s} \cdot \frac{\hat{F}}{m_{tot}}\end{aligned}$$

$$\begin{aligned} \Rightarrow \hat{x} &= \frac{K_1 + K_2 \cdot s}{s^2 + K_2 \cdot s + K_1} \cdot x + \frac{\hat{F}/m_{tot}}{s^2 + K_2 \cdot s + K_1} \\ \Rightarrow x - \hat{x} &= x - \frac{K_1 + K_2 \cdot s}{s^2 + K_2 \cdot s + K_1} \cdot x - \frac{\hat{F}/m_{tot}}{s^2 + K_2 \cdot s + K_1} \\ \Rightarrow x - \hat{x} &= \frac{s^2 + K_2 \cdot s + K_1}{s^2 + K_2 \cdot s + K_1} \cdot x - \frac{K_1 + K_2 \cdot s}{s^2 + K_2 \cdot s + K_1} \cdot x - \frac{\hat{a}}{s^2 + K_2 \cdot s + K_1} \end{aligned}$$

where $\hat{a} = \frac{\hat{F}}{m_{tot}}$

$$\begin{aligned} \Rightarrow x - \hat{x} &= \frac{s^2}{s^2 + K_2 \cdot s + K_1} \cdot x - \frac{\hat{a}}{s^2 + K_2 \cdot s + K_1} \\ \Rightarrow x - \hat{x} &= \frac{a}{s^2 + K_2 \cdot s + K_1} - \frac{\hat{a}}{s^2 + K_2 \cdot s + K_1} \end{aligned} \quad (4.4)$$

where $a = s^2 \cdot x$

Velocity Observer - Discrete Time

The velocity observer, as detailed in the previous section, uses a model of a second order plant to estimate both motor position and velocity, which leads us to the following discrete time observer plant model [13]:

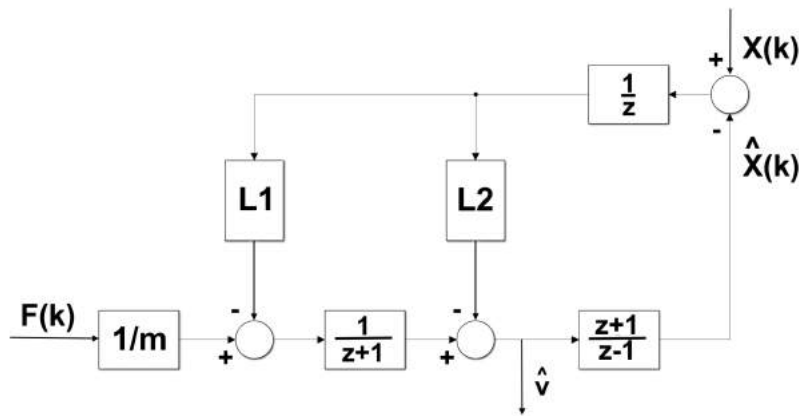


Figure 4.12: Discrete Observer Block Diagram [13].

where an extra delay element is introduced into the observer's error path to overcome the algebraic loop in the feedthrough path of the block $\frac{z+1}{z-1}$.

One can derive, as before, an expression for \hat{x} neglecting the feedforward term:

$$\hat{x} = \frac{z+1}{z-1} \cdot \left[\frac{L_1}{z} \cdot \frac{(x-\hat{x})}{z-1} + \frac{L_2}{z} \cdot (x-\hat{x}) \right]$$

$$\implies \hat{x} = \frac{L_2 \cdot z^3 + (L_1 - L_2) \cdot z + L_1}{z^3 + (L_2 - 2) \cdot z^2 + (L_1 + 1) \cdot z + L_1 - L_2} \quad (4.5)$$

The closed-loop observer gains determine the observer dynamics and define the poles. The system is of third-order due to the presence of a delay in the error path. As a consequence it is difficult to derive an equivalence between the gains of the discrete third-order system and the continuous second-order system.

Choosing L_1 and L_2

Considering the open-loop transfer function of the observer's inner and outer loops, it is possible to choose L_1 and L_2 . According to [13], three possible sets of gains are listed below:

Observer Gains		
Set	L_1	L_2
Low	0.01125	0.10
Medium	0.024726	0.1715728
High	0.035	0.3

Table 4.3: Observer Gain Values.

The observer gain selection is a compromise between noise filtering (high) and better disturbance rejection (low).

The primary purpose of this work is to reduce the noise, so that the medium and the high sets will be considered.

The results of the simulation are:

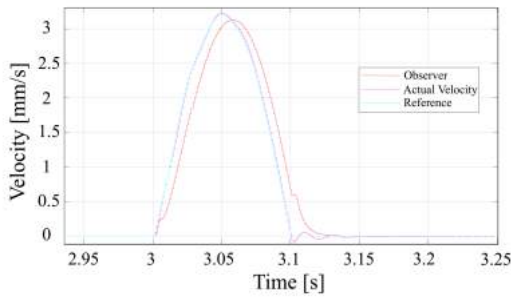


Figure 4.13: Simulation Velocity Plot (Hard).

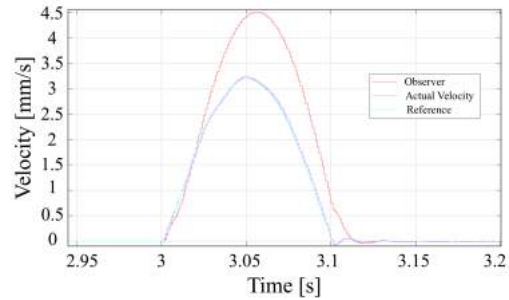


Figure 4.14: Simulation Velocity Plot (Medium).

It is clear that the observer estimation in Figure 4.13 has a large delay, therefore every change in speed will be seen later by the controller. Conversely, the observer estimation in Figure 4.14 reacts faster, so that the medium set is chosen as an acceptable compromise between noise filtering and disturbance rejection. It is important to notice that an overestimation of the velocity, as can be seen in Figure 4.14, is not an issue, but it is actually helpful in terms of response time. As a matter of fact, one can see an improvement in the noise level in the displacement from Figure 4.15 to Figure 4.16. The standard deviation, evaluated in the two cases, improves from 16.9 nm (velocity estimated by derivative) to 9.7 nm (velocity estimated by observer).

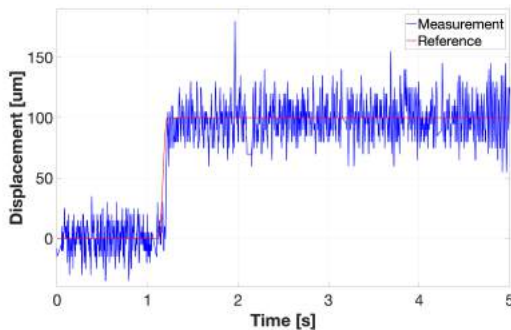


Figure 4.15: 100 nm displacement, velocity estimated by derivative.

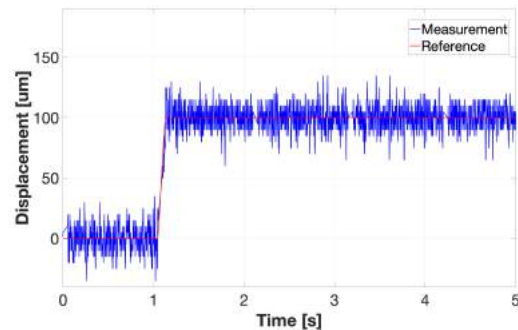


Figure 4.16: 100 nm displacement, velocity estimated by observer.

Finally, the simulink control block is displayed below:

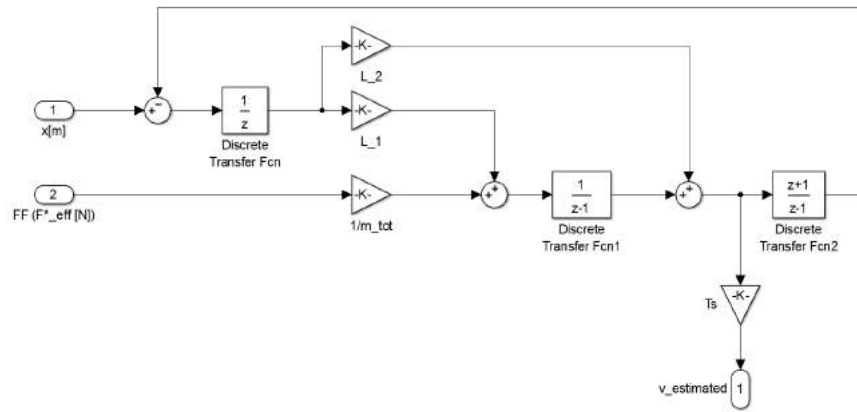


Figure 4.17: Discrete Observer, Simulink Block Diagram.

Chapter 5

NONLINEAR CONTROL

In this chapter, the control algorithm presented in the previous chapter will be improved in order to allow the positioner to work in the nonlinear range. The use of the simple linear model, as in [3.3](#), is efficient and gives good results only inside a small range of operation (up to 0.2 mm). To control the manipulator in a range of up to 1 mm, it is essential to take into account the nonlinearities of the system. The nonlinear model has already been presented in section [3.2](#). The stiffness, and so the force required, drastically increases with the displacement so that it cannot be neglected beyond 0.2 mm. Hence, the stiffness has no longer a constant value, but the nonlinear function reported in equation [3.10](#). This function gives the instantaneous value of stiffness based on the actual position.

5.0.1 Feedback Control

In the feedback control, it may be necessary to make a correction of the instantaneous error. This means that if the instantaneous stiffness is known, it becomes possible to evaluate the required force to correct the position error. As mentioned above, the instantaneous value of the stiffness can be calculated. Therefore, the control strategy can be simply updated replacing

the constant stiffness gain with a variable gain which varies with the actual position, according to equation [3.10](#). In Simulink, this variable gain can be implemented through a matlab function; the relative matlab code is displayed in Appendix [C](#)

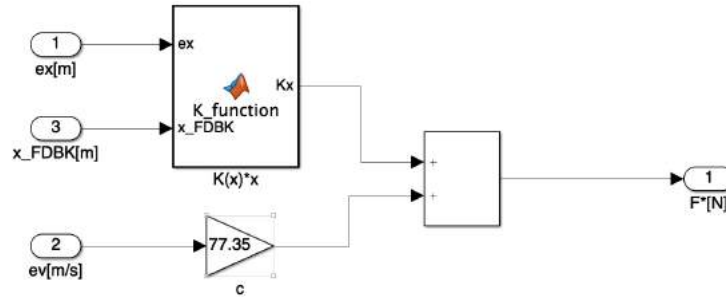


Figure 5.1: Nonlinear Feedback Control Simulink Block Diagram.

In Figure [5.1](#) it can be noticed that the matlab function has two inputs: the position error (e_x) and the position feedback (x_{FDBK}) from the encoder. The first one is used to evaluate the force needed and the latter is used to calculate the instantaneous stiffness. The result of the block (Kx) is the elastic force, which is summed with the viscous force where c is the damping coefficient and ev is the velocity error. In a mathematic form, this can be written as:

$$F_{el}^{inst} = k(x_{FDBK}) \cdot e_x \quad (5.1)$$

5.0.2 Feedforward Control

For the feedforward control, it is necessary to predict the required force, based on the references. Hooke's law states that the absolute value of the elastic force is simply $|F_{el}| = k \cdot |x|$, but this equation is true only as long as the stiffness is constant. The stiffness of the nanopositioning system changes with the displacement and therefore one cannot use Hooke's law, i.e. $|F_{el}| \neq |k(x) \cdot x|$.

The general formula for the elastic force is:

$$F_{el} = \int k(x) \cdot dx \quad (5.2)$$

From equation 5.2, it is trivial to compute Hooke's law when supposing a constant stiffness. However, the result is different if k is a function of the position.

The stiffness function is known and, as in the elastic force equation, see equation 3.9, hence it is not necessary to perform any integration. The control strategy can be updated replacing the constant stiffness gain with a Matlab function implementing the force equation 3.9 (the relative Matlab code is reported in Appendix D). The Simulink block diagram designed for the feedforward control is reported in Figure 5.2.

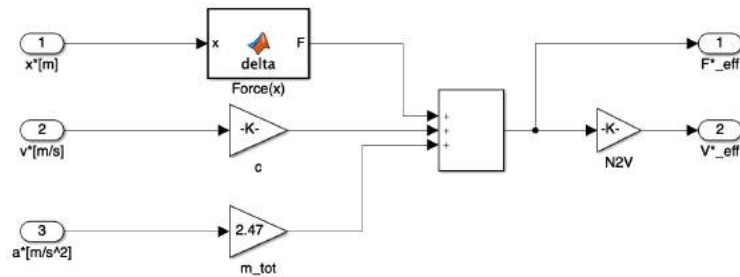


Figure 5.2: Simulink Block Diagram for Nonlinear Feedforward Control.

5.1 Nonlinear Range Test Results

In this section the experimental tests, carried out within this thesis, are reported. The results shown, were performed using the nonlinear control algorithm with the velocity observer (see Chapter ??). The first section reports the tests about the response and the maximum error of the control developed for a s-curve position profile input in the entire range (up to 1 mm). Before displaying the test results, it is worth to specify the direction of a positive displacement, as indicated in Figure 5.3:

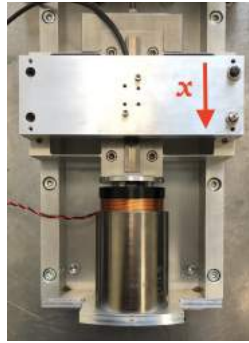


Figure 5.3: Positive Displacement Direction.

Therefore, if the actuator pulls (positive current flowing into it) we have a positive displacement encoder-wise, and vice versa.

In order to study the response of the control, several s-curve position profiles were applied, maintaining the position variation until the steady state was reached. At the same time, the instantaneous error with respect to the reference was tracked. Using the control algorithm developed, based on the theoretical model, the results reported in Figures [5.4](#)-[5.9](#) were obtained.

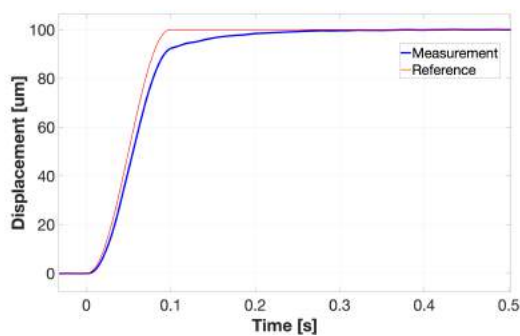


Figure 5.4: Pre-Tuning Non-linear Control, 0.1 mm displacement (Rise Time = 0.1 s).

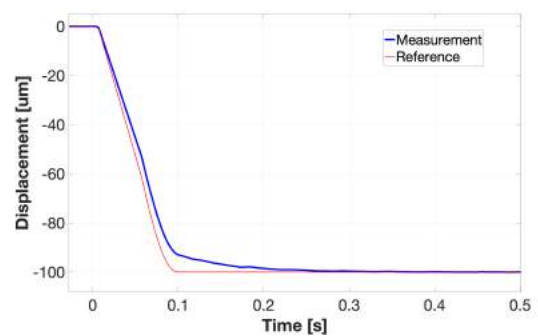


Figure 5.5: Pre-Tuning Non-linear Control, -0.1 mm displacement (Rise Time = 0.1 s).

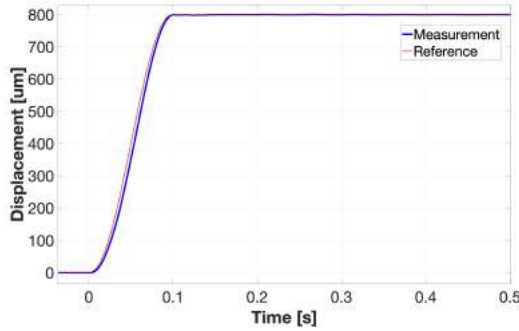


Figure 5.6: Pre-Tuning Non-linear Control, 0.8 mm displacement (Rise Time = 0.1 s).

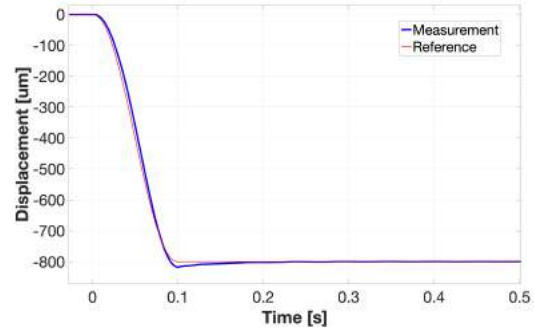


Figure 5.7: Pre-Tuning Non-linear Control, -0.8 mm displacement (Rise Time = 0.1 s).

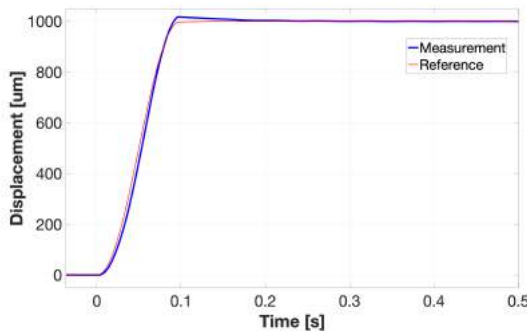


Figure 5.8: Pre-Tuning Non-linear Control, 1 mm displacement (Rise Time = 0.1 s).

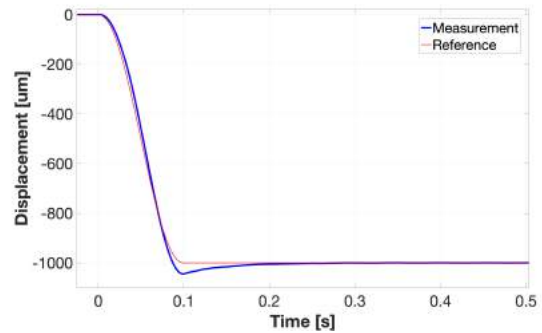


Figure 5.9: Pre-Tuning Non-linear Control, -1 mm displacement (Rise Time = 0.1 s).

As can be seen, the control is quite inaccurate, with large errors, both positive and negative depending on the displacement required. It is clear that the feedforward "guess" underestimates the force required in the linear range and overestimates the force in the nonlinear range. In order to improve the feedforward guess, the theoretical force law (3.18) required to be tuned. To do so, 0.1 mm and 1 mm displacements were used as tuning pivots in both directions. As a matter of fact, it is known that 0.1 mm is in the linear range of the curve, where the x term is preponderant. On the other hand, 1 mm is in the nonlinear range where the x^3 term is prevalent.

The generic modified law is:

$$F_y = \left(\frac{48 \cdot E \cdot I}{L^3} + k_{XYZ} + \text{error}L \right) \cdot Y_S + \frac{\text{error}N \cdot E \cdot I}{\frac{L^5}{d} + \frac{L^3}{700} \cdot Y_S^2} \cdot Y_S^3 \quad (5.3)$$

By considering several tests, it was possible to experimentally tune $\text{error}L$ (looking at 0.1 mm displacements) and $\text{error}N$ (looking at 1 mm displacements). The correction factors evaluated are:

Positive Range (+x):

- $\text{error}L = 2.5432 \text{ e4 N} \cdot \text{m}^{-1}$
- $\text{error}N = 1.6$

Negative Range (-x):

- $\text{error}L = 2.19 \text{ e4 N} \cdot \text{m}^{-1}$
- $\text{error}N = 1.18$

The final test results are reported in Figures [5.10](#)[5.15](#).

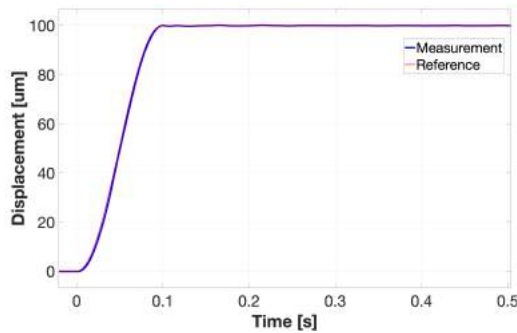


Figure 5.10: Post-Tuning Non-linear Control, 0.1 mm displacement (Rise-time = 0.1 s).

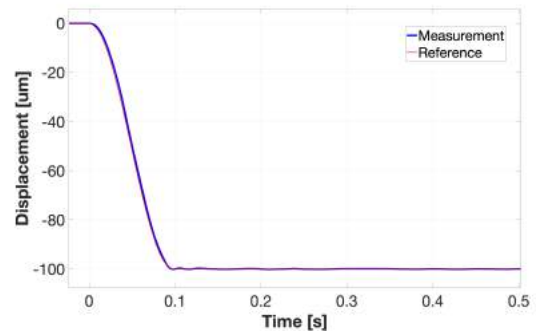


Figure 5.11: Post-Tuning Non-linear Control, -0.1 mm displacement (Rise-time = 0.1 s).

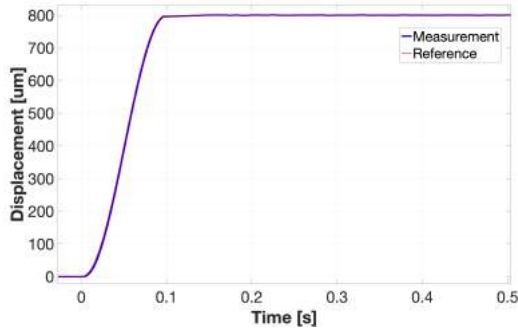


Figure 5.12: Post-Tuning Non-linear Control, 0.8 mm displacement (Rise-time = 0.1 s).

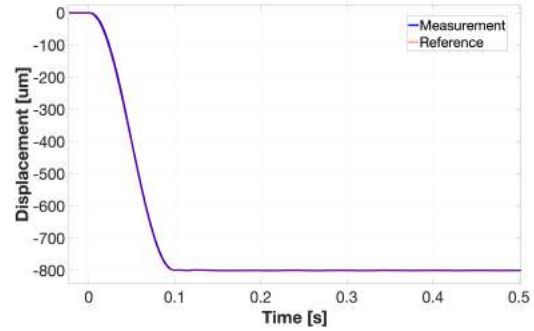


Figure 5.13: Post-Tuning Non-linear Control, -0.8 mm displacement (Rise-time = 0.1 s).

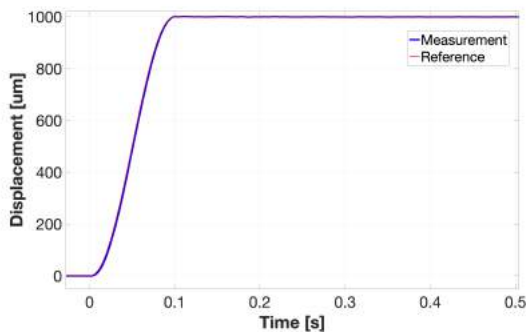


Figure 5.14: Post-Tuning Non-linear Control, 1 mm displacement (Rise-time = 0.1 s).

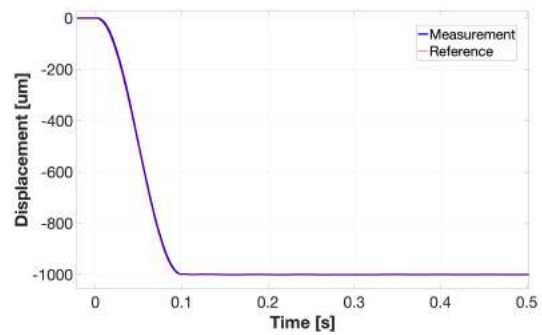


Figure 5.15: Post-Tuning Non-linear Control, -1 mm displacement (Rise-time = 0.1 s).

The tuning of equation [5.3](#) allows to achieve a high level of accuracy in the considered range of $[-1;1]$ mm. In order to quantify the improvements achieved, the maximum transient errors are shown in Table [5.1](#) (no error is expected in steady state).

Errors				
Displacement Absolute Value [mm]	Pre – Tuning Positive	Post – Tuning Positive	Pre – Tuning Negative	Post – Tuning Negative
0.1	+10% (10 μm)	+2.5% (2.5 μm)	> -9% (9 μm)	-2.5% (2.5 μm)
0.8	+6% (48 μm)	< +2% (16 μm)	+2.5%, > -5% (40 μm)	< -2% (16 μm)
1	> +6.5% (65 μm)	< +2% (20 μm)	> $\pm 4.5\%$ (45 μm)	< -2% (20 μm)

Table 5.1: Error Comparison Between the Pre- and Post- Tuning Force Law.

The two laws for the actuation force, the pre- and the post- tuning, have been plotted together for comparison in Figure 5.16.

At this point, the required force to perform a displacement is clear, so that the maximum range can be reconsidered taking into account the available actuation force. The voice coil actuator (LA30-48-000A BEI) imposes limits which, according to the datasheet, are:

- **Peak Force** = 445 N
- **Continuos Stall Force** = 133.8 N

From the post-tuning equation 5.3 one gets:

- $|F(0.817e-3)| = 133.805$ N
- $|F(1.8473e-3)| = 445.00$ N
- $|F(-0.92115e-3)| = -133.805$ N
- $|F(-2.0075e-3)| = -445.03$ N

As a comparison, the force values of the pre-tuning law (3.18) are displayed:

- $|F(\pm 0.8867e-3)| = 133.803$ N
- $|F(\pm 1.6577e-3)| = 445.01$ N

The force values evaluated so far neglect the *dynamic force*¹. Additionally, it is clear that the previous range [-2.2, 2.2] mm, which took into account just the mechanical constraints (see paragraph 3.2.4), is unrealistic. Within that range, [-1, 1] mm it is already beyond the continuous stall force limit, but it is well under the peak force limit; thus, this range could be considered a more realistic range for the robot having a good margin for dynamic control. It is important to highlight that such range is considered to be excellent for a nano-positioning robot.

The control algorithm discussed above is able to move the manipulator inside the range [-1, 1] mm, without overshoots thanks to the enhanced feedforward. The feedforward was corrected by experimentally tuning the theoretical force law, which did not take into account the imperfections of the system analyzed, such as the dimensional tolerances. However, it is worth emphasizing the approach used to enhance the feedforward itself, because it can be used to improve the control of a similar manipulator with different imperfections.

¹dynamic force refers to the forces required to perform a movement (for a given acceleration and velocity). The force is zero in static conditions:

$$F_{dynamic} = \text{Mass} * \text{Acceleration} + \text{Damping Coefficient} * \text{Velocity}$$

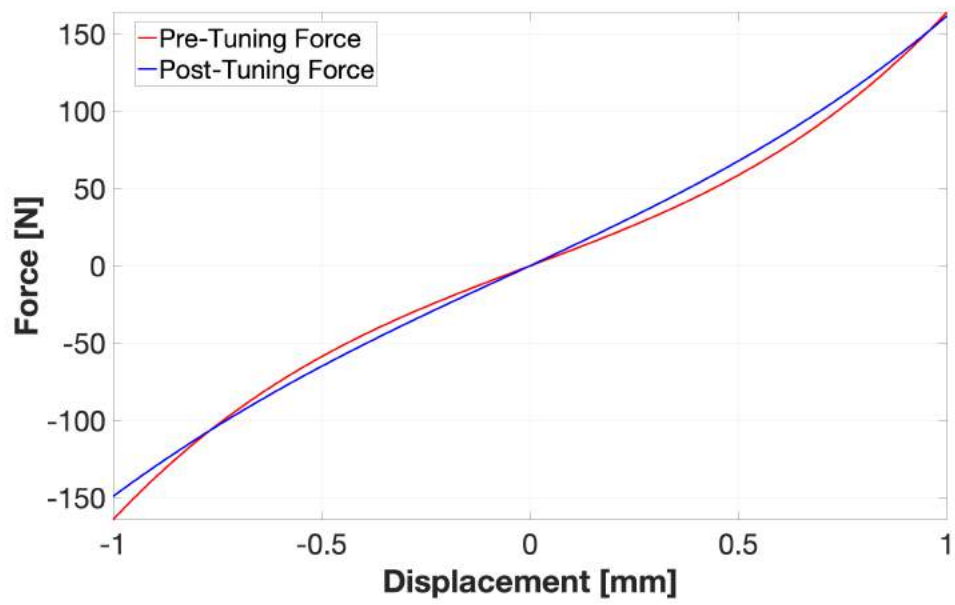


Figure 5.16: Pre- and Post- Tuning Comparison of the Force Magnitude within 1 mm Range.

Chapter 6

DYNAMIC ANALYSIS

This chapter analyzes the resonant behaviour of the system in dynamic conditions for small displacements ($\ll 0.2$ mm), where the system can be considered linear. In order to analyze the resonances of the closed-loop system, a sinusoidal waveform was applied with variable frequency (variation 1 Hz per s), see Figure [6.1](#).

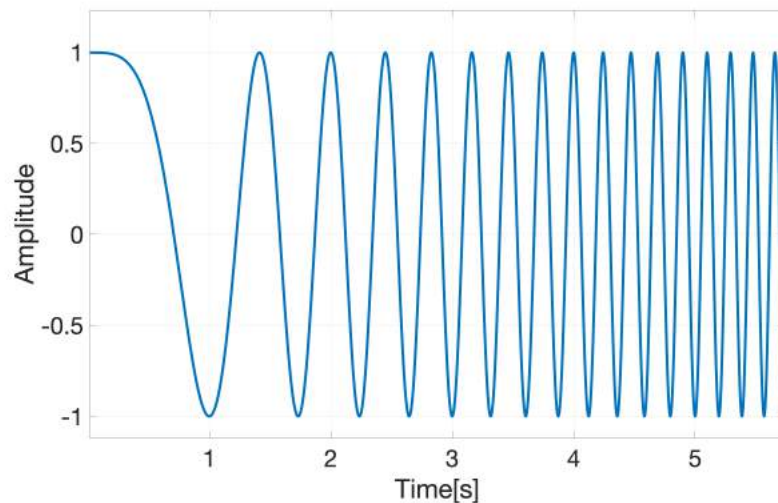


Figure 6.1: Example of a Sinusoidal Waveform with Variable Frequency, variation of 1 Hz per s.

The frequency varies from 0 to 300 Hz (to avoid excessive aliasing, given

that the sampling time is 1 ms). The red plot in Figure 6.2 is the reference, while the blue one is the response of the system.

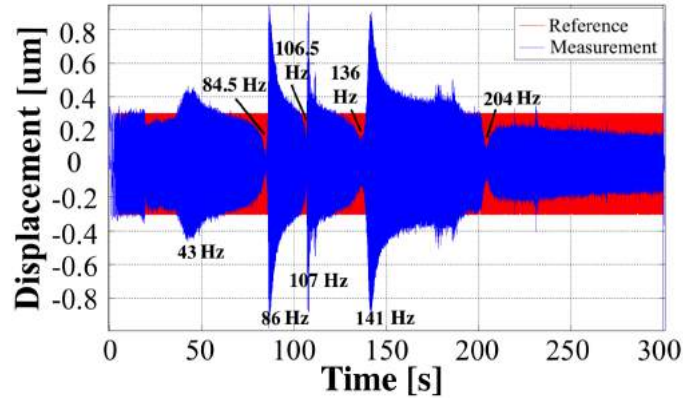


Figure 6.2: Sinusoidal Waveform Reference with Variable Frequency, 0 Hz to 300 Hz (1 Hz/s), Amplitude 300 nm.

Knowing the rate of change of frequency (in this case 1 Hz/s), it is clear that an estimate of the instantaneous frequency can be inferred from the time axis. Hence, the time axis was replaced by an equivalent frequency axis, as can be seen in Figure 6.2. It is still a time response and not a frequency one, but the figure gives a pretty good idea where the resonances are in the spectrum.

As expected, the frequency behaviour remains unchanged in other tests in the same frequency range with different frequency changing rates and/or if an inverse sinusoidal waveform input (300-0 Hz) is utilized.

From [19] it is clear that the first order resonance is at

$$\omega_n = 266.413 \text{ rad} \cdot \text{s}^{-1} = 42.4 \text{ Hz.}$$

This value is in agreement the experimental result reported in Figure 6.2, where the first resonance is around 43 Hz.

From Figure 6.2, several resonances can be seen within the range 0-200 Hz; such a large number of resonances so close to each other are hard to ascribe to real resonances of the system. Indeed, only the aforementioned

first one is theoretically justified.

In order to understand the influence of different components on the system, some parts were disconnected and individually analyzed. It was found that:

- the resonance at frequency 43 Hz is ascribed to CBPM;
- the resonance at frequency 86 Hz is caused by a loose connection between the stages (solved by tightening the screws);
- the resonance at frequency 107 Hz is due by the end-effector¹ (solved by removing it).

Applying the solutions above, the result reported in Figure 6.3 is obtained.

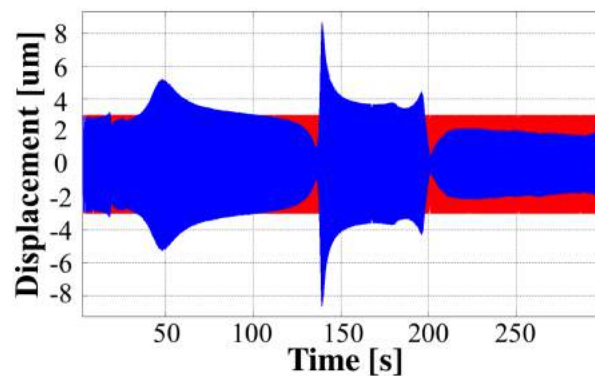


Figure 6.3: Sinusoidal Waveform Reference with Variable Frequency, 0 Hz to 300 Hz (1 Hz/s), Amplitude 3 μm without end effector and tightened connection.

¹a square metal plate on top of the XYZ stage without a real purpose in the current set-up, see Section 2.1.2

6.1 Rate Limiter Function Block

Testing different amplitudes for the same variable frequency sine wave, an unexplained behaviour showed up for amplitudes greater than $10\ \mu\text{m}$, and above 180 Hz, as can be seen in Figure 6.4:

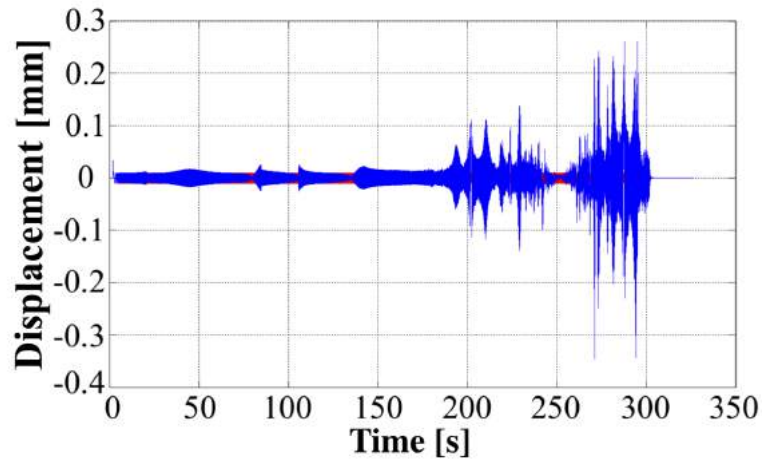


Figure 6.4: Sinusoidal Waveform Reference with Variable Frequency, 0 Hz to 300 Hz (1 Hz/s), Amplitude $10\ \mu\text{m}$.

This behaviour turned out to be due by the rate limiter² in the control algorithm that was set up with a couple of simplifications; one of them was the assumption of negligible dynamic force ($m \cdot \ddot{x} + c \cdot \dot{x} \ll k \cdot x$), but this is no longer true. As a matter of fact, by removing the rate limiter, the behaviour gets back to that expected.

The rate limiter had been included in order to avoid a speed higher than 0.135 m/s, above which the encoder is not capable of measuring the position correctly. Therefore, it is necessary to evaluate the limits introduced by the encoder to ensure accurate control.

²the rate limiter is a control block provided by the Simulink library which was introduced by a former student who was working on the same project, for more details about it check section 5.1 of [18]

A rate limiter which takes into account dynamic conditions is not possible, therefore the frequency should be correlated with the velocity in order to understand when the encoder could be an issue.

Let's consider a generic sinusoidal waveform as in Figure 6.5 (T = period):

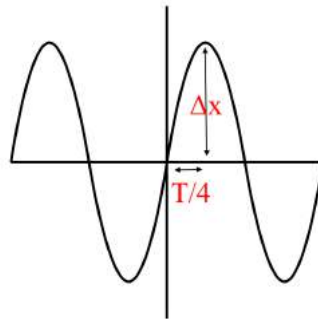


Figure 6.5: Sinusoidal Waveform.

Thus, it is possible to link the speed and the frequency as follows:

$$velocity = \frac{\Delta x}{\Delta t} = \frac{\Delta x}{T/4} = 4 \cdot \Delta x \cdot f \quad (6.1)$$

The chart that shows the maximum frequency manageable by the encoder in function of the displacement is reported in Figure 6.6.

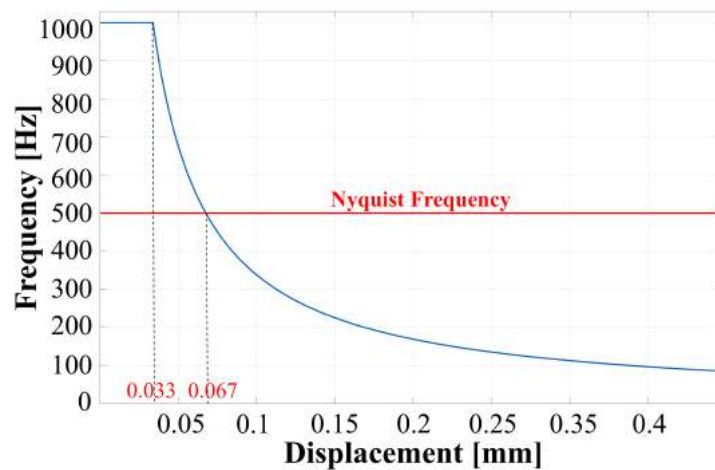


Figure 6.6: Plot of the frequency limit in function of the displacement, where

$$f = \frac{0.135}{4 \cdot \Delta x}.$$

In Figure [6.6](#), the output has been limited to 1 kHz and the red line is the Nyquist Frequency due to the sampling time of the dSPACE controller. As can be seen from Figure [6.6](#), the encoder does not limit the frequency under 1 kHz for displacements smaller than 33 μm and it does not limit the system beyond the Nyquist frequency for displacements smaller than 67 μm .

In conclusion, it is clear that the encoder is not a real limit since the actuation power limit is stricter for relatively large displacements and the Nyquist limit is the bottleneck for small displacements. Therefore, the rate limiter was removed and no other changes were carried out.

6.2 Analysis of the Resonances

There is still an unexpected resonant behaviour between $\approx 140 - 200$ Hz, as it is evident from Figure [6.3](#). This resonance is not due to the XYZ stage because it was present even when the stage had been disconnected from the CBPM. Therefore, it could be supposed the CBPM to be the cause. However, there was no logical explanation based on theory nor on an imperfection in the structure, like a loose connection, which could have justified the aforementioned resonant behaviour.

A further test revealed that this vibration was due to the base frame itself (theoretically a static structure); to show that, the inertia of the base frame was increased, overlapping some ballast on the fixed parts and, as can be seen in Figure [6.7](#), the resonant behaviour was highly reduced.

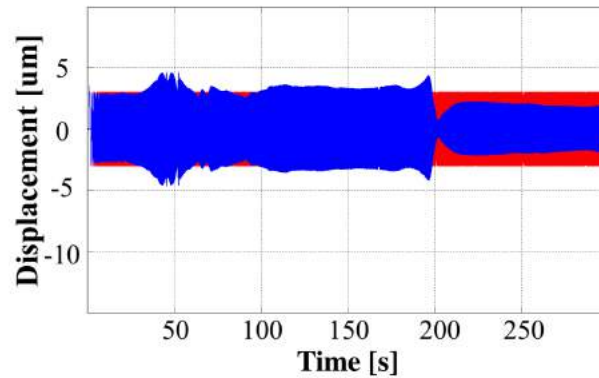


Figure 6.7: Sinusoidal Waveform Reference with Variable Frequency, 0 Hz to 300 Hz (1 Hz/s), Amplitude 3 μm , improved inertia.

In order to improve the rigidity of the manipulator in a permanent manner, the base frame was clamped sideways; see Figure 6.8. The final response is shown in Figure 6.9, below:

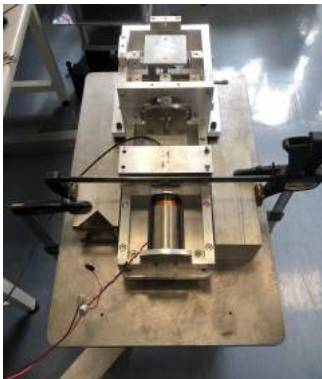


Figure 6.8:
Clamped Base Frame.

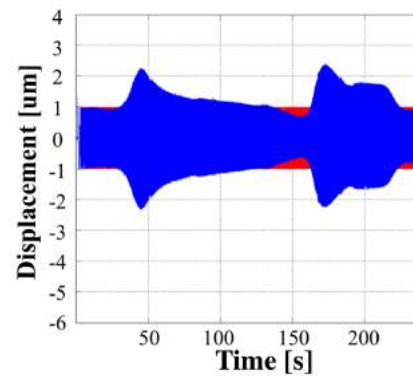


Figure 6.9:
Response of Clamped System.

It is clear that the antiresonances are almost gone and the peak value of the vibration is reduced.

6.3 New Model

Analyzing Figure 6.3, the system seems to be limited frequency-wise above 200 Hz (Figure 6.2); this behaviour cannot be ascribed to the encoder, to the Nyquist frequency, nor to power limit.

Instead, it is due to an inaccurate model of the nano-positioning system.

The current model in the linear range³ is (as explained in Chapter 3)

$$\frac{X(s)}{V(s)} = \frac{35.14}{1.824 \cdot s^2 + 22.353 \cdot s + 129460} \quad (6.2)$$

where $m_{tot} = 1.824 \text{ kg}$, $c = 22.353 \text{ kg}^{\frac{1}{2}} \cdot \text{N}^{\frac{1}{2}} \cdot \text{m}^{-\frac{1}{2}}$, $k = 129460 \text{ N} \cdot \text{m}^{-1}$

In order to evaluate a new model, the System Identification Toolbox developed by Lennart Ljung [25] was used (integrated in Matlab).

Two different data sets were collected, one generated by a variable sinusoidal input, like the one used previously and reported in Figure 6.10, and one generated by a pseudorandom binary sequence (PRBS), see Figure 6.11. Both sets were collected by applying the input in a completely open-loop and control-free manner, in order to have a direct correlation between input (force) and output (position).

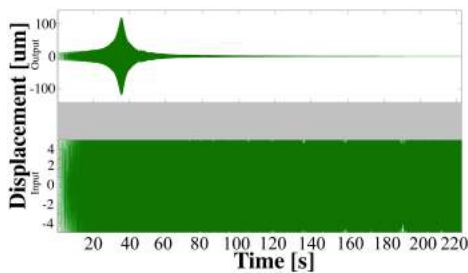


Figure 6.10: Variable Sinusoidal output-input.

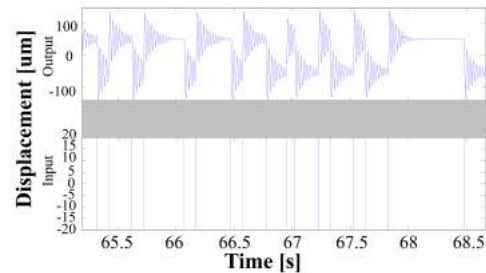


Figure 6.11: PRBS output-input.

The continuous second order system without zeros obtained using the PRBS data set as Working Data (fit 82.94%) and the sinusoidal data set as

³the dynamic tests are limited to a small range where the nonlinearities can be neglected

Validation Data⁴ (fit 72.98%) is:

$$\frac{X(s)}{V(s)} = \frac{14.2}{s^2 + 30.45 \cdot s + 5.595e04} \quad (6.3)$$

Rewriting the equation similarly to equation 6.2, this gives:

$$\frac{X(s)}{V(s)} = \frac{35.14}{2.47 \cdot s^2 + 77.35 \cdot s + 138459} \quad (6.4)$$

From this, we can extrapolate new equivalent coefficients even if they do not have a proper physical meaning:

$$m_{tot} = 2.47 \text{ kg}, c = 77.35 \text{ kg}^{\frac{1}{2}} \cdot \text{N}^{\frac{1}{2}} \cdot \text{m}^{-\frac{1}{2}}, k = 138459 \text{ N} \cdot \text{m}^{-1}$$

Experimental results as reported in Figure 6.4.

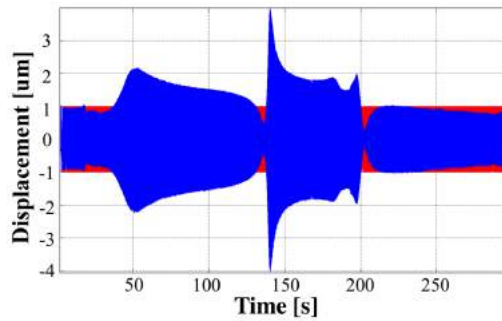


Figure 6.12: Sinusoidal Waveform Reference with Variable Frequency, 0 Hz to 300 Hz (1 Hz/s), Amplitude 1 μm , new model 6.4.

The improvement in the frequency above 200 Hz is clear. A new test keeping the original value of the stiffness revealed no significant changes, as can be seen in Figure 6.13, which means that the control can be updated with the new equivalent mass and viscous friction, while preserving the original stiffness value.

⁴check 25 for more details about Working and Validation Data

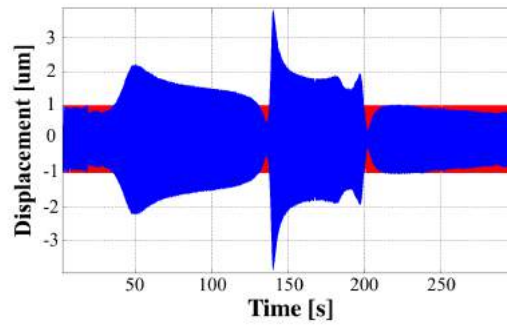


Figure 6.13: Sinusoidal Waveform Reference with Variable Frequency, 0 Hz to 300 Hz (1 Hz/s), Amplitude 1 μm , new model with original stiffness.

6.3.1 Bode Plot

It is possible now to compare the frequency response of the two models (equation [6.2](#) & equation [6.4](#), with $k = 129460 \text{ N} \cdot \text{m}^{-1}$):

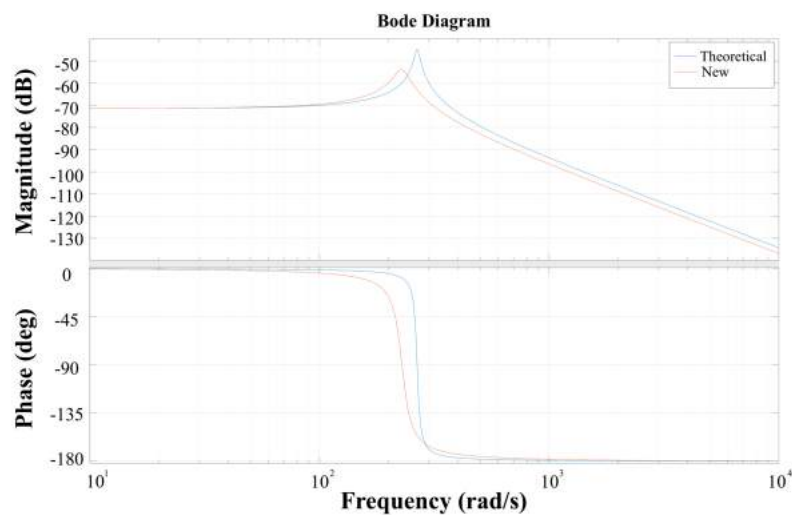


Figure 6.14: Bode Plot old ([6.2](#)) vs new model ([6.4](#)).

The new model shows its resonance in a lower frequency with a smoother peak.

6.3.2 Dynamic Characterization and Control

Accomplishments

The dynamic behaviour up to 300 Hz has been fully characterized and improved as much as possible. Furthermore, the new model identified enhances the ability of the control to follow the reference after 200 Hz. The possibility to reach higher frequencies (above 300 Hz) is constrained by the sample time which is limited by the CPU power.

The clamped layout of the system showed a sizeable improvement, limiting the resonances which could be further enhanced by a redesigned base frame.

This page is intentionally left blank.

Chapter 7

ANALYSIS OF CROSS-COUPLING

One of the main design requirements in compliant nano-manipulating systems is the motion accuracy. Compliant mechanisms can provide motions with high repeatability because they are free of backlash. However, due to the stiffness characteristics of compliant mechanisms, they typically suffer from cross-axis coupling which affects their motion accuracy.

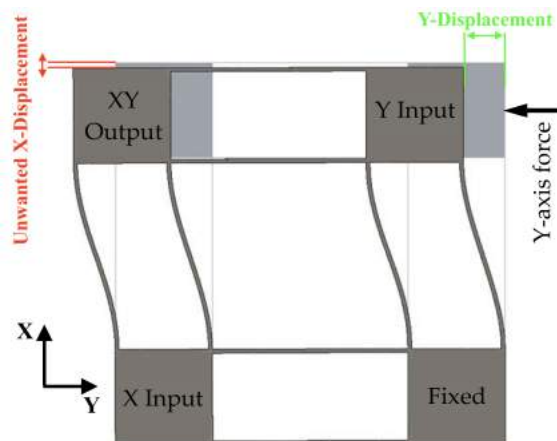


Figure 7.1: Cross-Axis Coupling Along the X-axis in a Compliant Mechanism

[5].

The cross-axis coupling in a multi-axis output stage is an unwanted motion interference along one DOF¹ direction caused by a motion, performed intentionally, along another DOF direction, as can be seen in Figure 7.1. This issue poses a challenge on large range XY compliant nano-manipulating systems to achieve the desired motion quality.

7.1 Four-Beam Compliant Module Actuation Forces

The multi-axis output stage of the manipulator analyzed so far is the XYZ CPM, previously presented in Section 2.1.2. A significant effect of the cross-axis coupling in the XYZ CPM is an increase of the actuation force required to perform a movement. In Section 3.2.5, the actuation force required was obtained for a single axis, neglecting the cross-axis coupling. In order to obtain a more accurate result, the complete symmetric XYZ CPM can be modelled based on the analytical model of the FBCM².

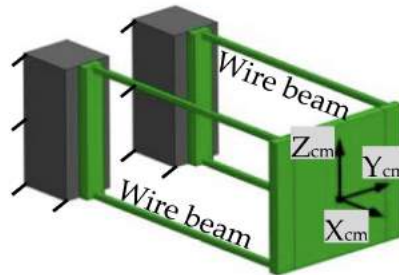


Figure 7.2: Four-Beam Compliant Module [5].

The analytical reaction forces produced by the deformation of the FBCM, as shown in Figure 7.2, were first reported in [26] and then applied to the XYZ CPM in [5]. The resultant actuation forces [7.1], [7.2] and [7.3] were obtained

¹Degree of Freedom

²Four-Beam Compliant Module

supposing that the primary translations are performed at very small velocities and, therefore, the dynamic contribution is negligible.

$$f_x = \frac{48 \cdot x_S \cdot (129 \cdot x_S^2 + 129 \cdot z_S^2 + 175 \cdot t^2)}{3 \cdot x_S^2 + 3 \cdot z_S^2 + 175 \cdot t^2} + \frac{48 \cdot x_S \cdot (129 \cdot x_S^2 + 129 \cdot y_S^2 + 175 \cdot t^2)}{3 \cdot x_S^2 + 3 \cdot y_S^2 + 175 \cdot t^2} + \frac{192 \cdot x_S \cdot (129 \cdot x_S^2 + 175 \cdot t^2)}{3 \cdot x_S^2 + 175 \cdot t^2} \quad (7.1)$$

$$f_y = \frac{48 \cdot y_S \cdot (129 \cdot y_S^2 + 129 \cdot z_S^2 + 175 \cdot t^2)}{3 \cdot y_S^2 + 3 \cdot z_S^2 + 175 \cdot t^2} + \frac{48 \cdot y_S \cdot (129 \cdot y_S^2 + 129 \cdot x_S^2 + 175 \cdot t^2)}{3 \cdot y_S^2 + 3 \cdot x_S^2 + 175 \cdot t^2} + \frac{192 \cdot y_S \cdot (129 \cdot y_S^2 + 175 \cdot t^2)}{3 \cdot y_S^2 + 175 \cdot t^2} \quad (7.2)$$

$$f_z = \frac{48 \cdot z_S \cdot (129 \cdot z_S^2 + 129 \cdot x_S^2 + 175 \cdot t^2)}{3 \cdot z_S^2 + 3 \cdot x_S^2 + 175 \cdot t^2} + \frac{48 \cdot z_S \cdot (129 \cdot z_S^2 + 129 \cdot y_S^2 + 175 \cdot t^2)}{3 \cdot z_S^2 + 3 \cdot y_S^2 + 175 \cdot t^2} + \frac{192 \cdot z_S \cdot (129 \cdot z_S^2 + 175 \cdot t^2)}{3 \cdot z_S^2 + 175 \cdot t^2} \quad (7.3)$$

where³

$f_i =$ normalized actuation force of the i – axis,

$i_S =$ normalized displacement of the i – axis,

$t =$ normalized thickness of the beam

The cross-axis coupling effect on the actuation forces is now clear and it is symmetrical thanks to the symmetry of the stage. The increase of the actuation force due to the cross coupling of the y-axis along the x-axis is:

$$\begin{aligned} \Delta f_x &= f_x(z_S = 0) - f_x(y_S = 0, z_S = 0) = \\ &= \frac{1058400 \cdot x_S \cdot y_S^2 \cdot t^2}{(3 \cdot x_S^2 + 3 \cdot y_S^2 + 175 \cdot t^2)(3 \cdot x_S^2 + 175 \cdot t^2)} \end{aligned} \quad (7.4)$$

³check Section 3.2.2 for the definition of normalized variables

where $f_x(z_S = 0)$ is the force along the x -axis due to displacements along the x - and y - axis and $f_x(y_S = 0, z_S = 0)$ is the force along the x -axis due to displacements along the x -axis. Therefore, Δf_x is the force along the x -axis due to displacements along the y -axis.

The equation [7.4](#) can be rewritten in actual terms as:

$$\Delta F_x = \frac{E \cdot I_{XYZ}}{\ell_{XYZ}^3} \cdot \frac{1058400 \cdot X_S \cdot Y_S^2 \cdot T_{XYZ}^2}{(3 \cdot X_S^2 + 3 \cdot Y_S^2 + 175 \cdot T_{XYZ}^2)(3 \cdot X_S^2 + 175 \cdot T_{XYZ}^2)} \quad (7.5)$$

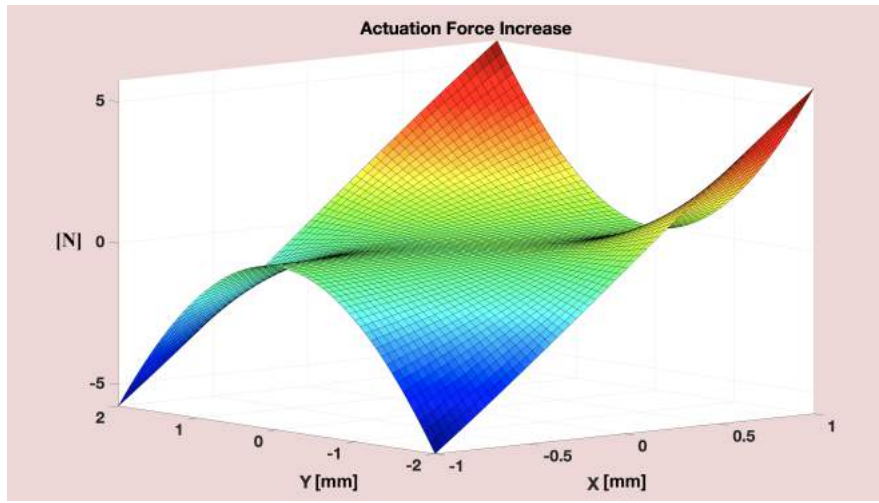


Figure 7.3: 3D plot of ΔF_x .

It is easy to see in Figure [7.3](#) that the increment is significant only when both the displacements along the two axes are enough large. Indeed, the surface in Figure [7.3](#) is flat with a value close to zero when at least one of the two displacements is small.

7.2 Test Results

In order to experimentally gauge the effect of the cross-axis coupling, several fixed displacements were applied by a precision screw along the y-axis. On the other hand, the x-axis displacements were applied by the control algorithm.

The data reported in Table 7.1 and plotted in Figures 7.4 and 7.5, were collected by an indirect measurement⁴ of the actuation force after the system had reached steady state. The tests were performed by varying the y-displacement from⁵ 0 to 2 mm for each x-displacement selected⁶. Three data sets were collected for each x-displacement and the regression line was evaluated. The linear fitting and the correlation coefficient (R) are displayed in Table 7.1.

The results reflect the trend seen in Figure 7.3, even though the values are slightly different. They shows an increase on the overall actuation force required to perform a movement smaller than 1% and always smaller than 3 N. It is important to highlight that the high stiffness of the CBPM conceals such force increment. Anyhow, when the displacement along the x-axis is small, the increase is highly negligible whatever the y-displacement is.

In conclusion, the cross-axis coupling between two axes is small enough to be neglected, whereas the feedback control is able to correct minor errors.

⁴using the equation 2.2 and the voltage value at the input of the "System" block (see Figure 4.5), it is possible to obtain an estimate of the force

⁵the y-displacement for each x-displacement selected are 0, 0.5, 0.6, 0.7, 0.8, 0.9, 1, 1.2, 1.4, 1.6, 1.8, 2

⁶the x-displacement selected are ± 0.05 , ± 0.1 , ± 0.2 , ± 0.4 , ± 0.6 , ± 0.8 , ± 0.9 , ± 1

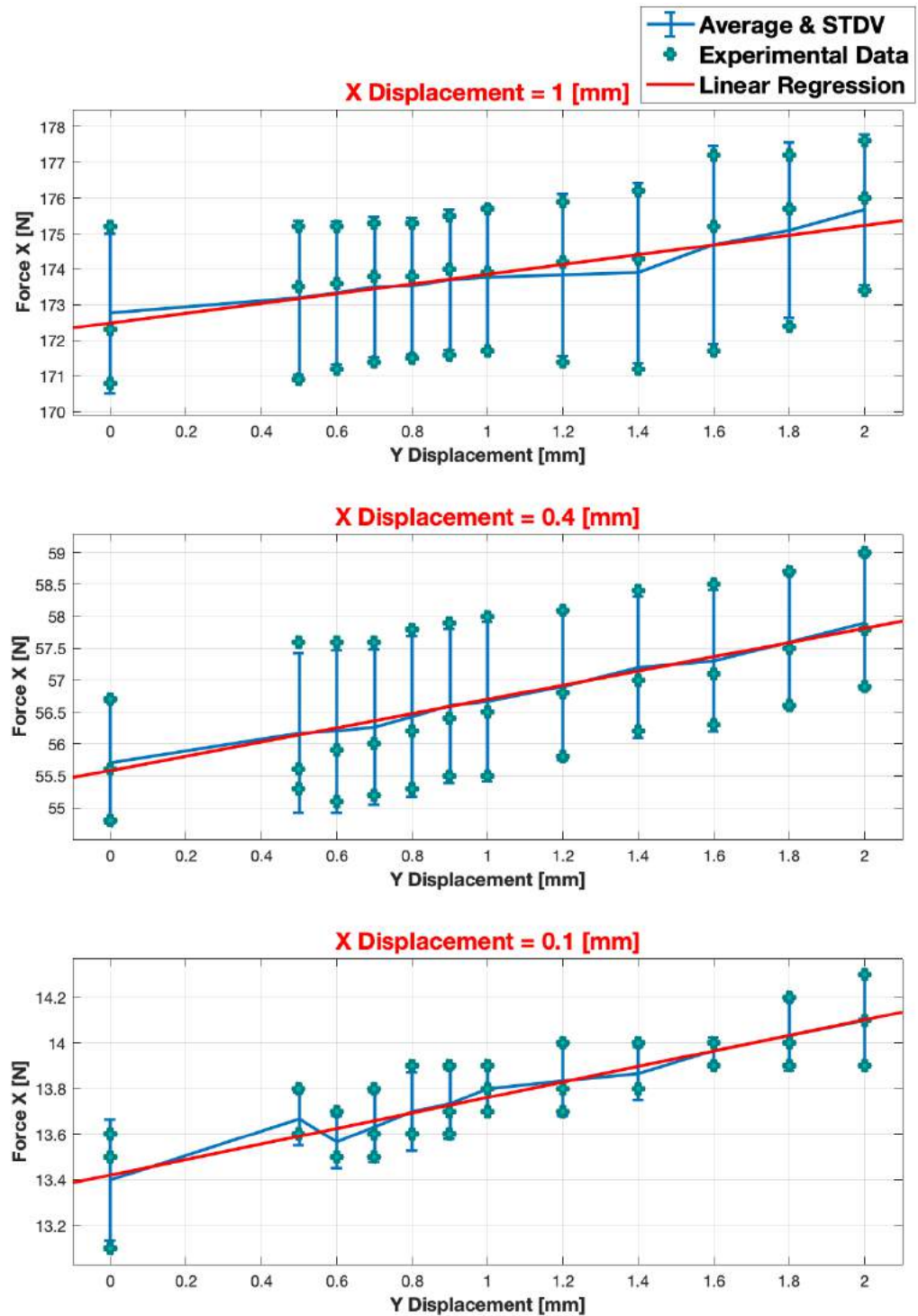


Figure 7.4: Cross-Axis Coupling Effect, Positive X-Axis Displacement.

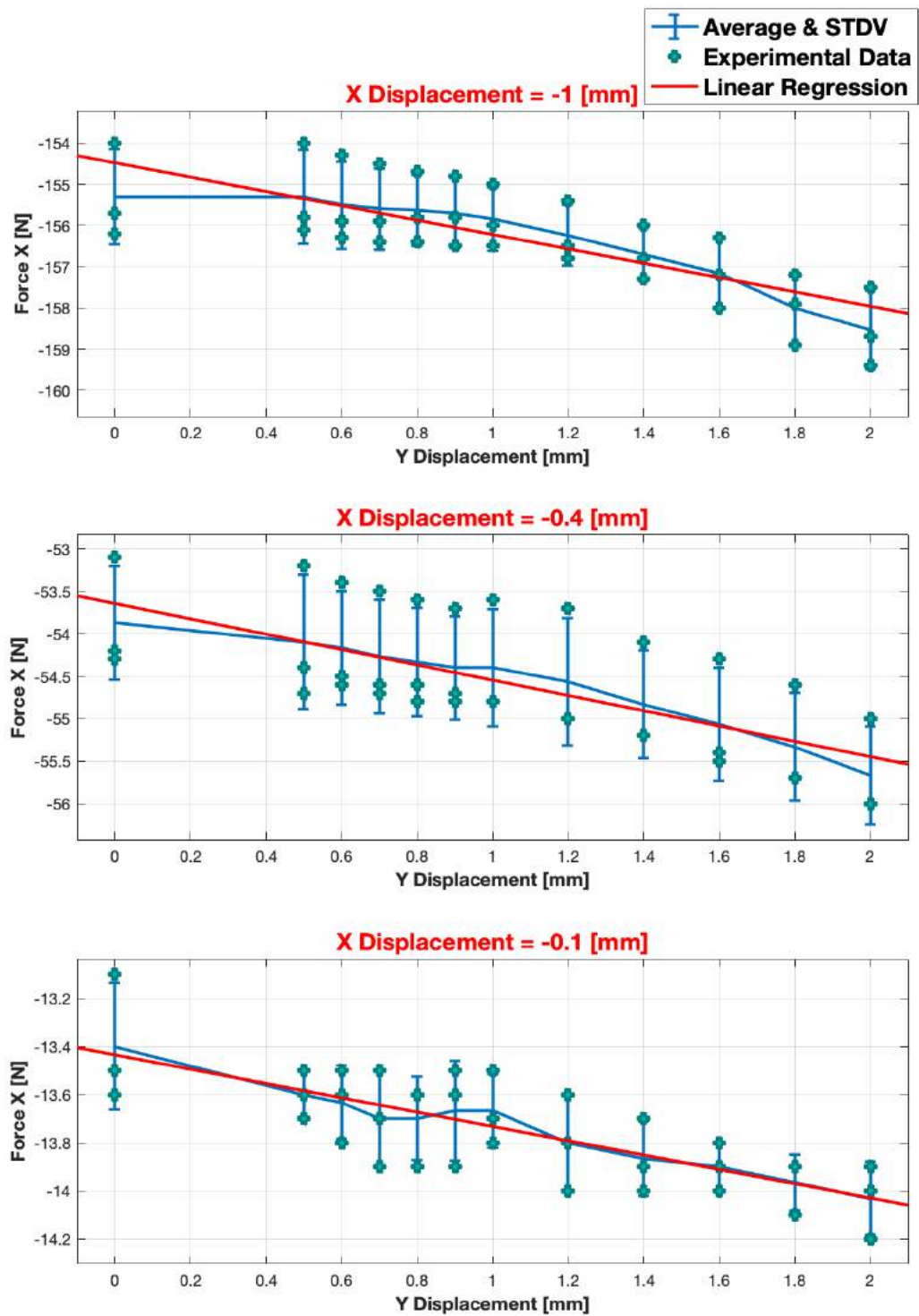


Figure 7.5: Cross-Axis Coupling Effect, Negative X-Axis Displacement.

Cross-Axis Coupling			
X [mm]	Linear	R	ΔF_x
Displacement	Fitting Line		@Y = 2mm
1 mm	$1.37 \cdot Y + 172.49$	0.96	2.74
0.9 mm	$1.41 \cdot Y + 148.13$	0.95	2.82
0.8 mm	$1.31 \cdot Y + 127.22$	0.98	2.62
0.6 mm	$1.36 \cdot Y + 88.38$	0.99	2.72
0.4 mm	$1.12 \cdot Y + 55.58$	0.99	2.24
0.2 mm	$0.61 \cdot Y + 26.75$	0.99	1.22
0.1 mm	$0.34 \cdot Y + 13.42$	0.98	0.68
0.05 mm	$0.16 \cdot Y + 6.90$	0.94	0.32
-1 mm	$-1.74 \cdot Y - 154.48$	0.93	3.48
-0.9 mm	$-1.80 \cdot Y - 134.65$	0.96	3.6
-0.8 mm	$-1.65 \cdot Y - 116.44$	0.96	3.3
-0.6 mm	$-1.53 \cdot Y - 82.79$	0.98	3.06
-0.4 mm	$-0.90 \cdot Y - 53.65$	0.97	1.8
-0.2 mm	$-0.55 \cdot Y - 26.55$	0.99	1.1
-0.1 mm	$-0.30 \cdot Y - 13.43$	0.98	0.6
-0.05 mm	$-0.12 \cdot Y - 6.96$	0.82	0.24

Table 7.1: Cross-Axis Coupling Force Effect Along the X-Axis.

CONCLUSIONS

A compliant nano-positioning system has been described, modeled and controlled in this thesis. The symmetry of the system allowed the analysis to be restricted to one of the three orthogonal translational axis of the device.

This thesis focused on three main objectives:

- Improving the closed-loop control with force feedforward, in order to reach the desired range of 1 mm, while taking into account the nonlinearities of the system.
- Analyzing the dynamic behaviour of the nano-positioning system and enhancing its capability by an improved model and setup.
- Assessing experimentally the cross-axis coupling effect between two axes.

The nonlinear model of the system was fully investigated from a theoretical point of view and integrated into the control algorithm. Subsequently, the effectiveness of the new control was tested and calibrated so that the desired motion quality was reached. Furthermore, the control was improved by the design of a velocity observer in order to achieve a less noisy velocity feedback.

The dynamic behaviour of the manipulator up to 300 Hz has been characterized and improved as much as possible. The new model identified enhances the ability of the control to follow the reference above 200 Hz, while the base frame was clamped in order to reduce the amplitude of the resonances of the

system.

Finally, the effect of the cross-axis coupling of the actuation force was examined through a significant number of tests. This last effect is small enough to be neglected, whereas the feedback control is able to correct minor errors.

Future Work

The characterization of the single axis has been complete. The next step is to add the required actuators on the other axes and to develop the control for multiple axes in order to allow accurate positioning over either 2D or 3D space.

In order to enhance the bandwidth, it will be necessary to substitute the current DSP with a more powerful one so that it will be possible to reduce the sample time required. Moreover, a more rigid base frame should be designed in order to further reduce the vibrations of the system.

Appendix A

Manipulator Parameter Values

Parameter	Symbol	Value	Unit of Measurement
Overall Mass	m_{tot}	1.824	kg
Damping Factor	ξ	0.023	/
Viscous Friction	c	22.353	$N^{\frac{1}{2}} \cdot kg^{\frac{1}{2}} \cdot m^{-\frac{1}{2}}$
Stiffness Linear Range	k_t	129,460	$N \cdot m^{-1}$
Young's Modulus, Al 6061-T6 (US)	E	69	GPa
CBPM Sheet Width	U	40	mm
CBPM Sheet Thickness	T	1	mm
CBPM Sheet Length	L	50	mm

CBPM Spanning Size	W	50	mm
CBPM Moving Stage Thickness	H	60	mm
CBPM Constant*	d	3E4	/
CBPM 2nd Moment of Area**	I	3.33	mm^4
XYZ CPM Beam Width	U_{XYZ}	1	mm
XYZ CPM Beam Thickness	T_{XYZ}	1	mm
XYZ CPM Beam Length	L_{XYZ}	50	mm
XYZ CPM 2nd Moment of Area**	I_{XYZ}	8.33E-2	mm^4
XYZ CPM Stiffness	k_{XYZ}	13,248	$N \cdot m^{-1}$
Voice Coil Force Sensitivity	k_f	35.14	$N \cdot A^{-1}$
Servo Amplifier Gain	k_d	1	$A \cdot V^{-1}$

Table A.1: Manipulator Parameter Values.

$$* d = \left(\frac{12}{(T/L)^2} \right)$$

$$** \text{ 2nd Moment of Area of Rectangles: } I = \left(\frac{1}{12} \cdot U \cdot T^3 \right)$$

Appendix B

S-Curve Profile Generator

Listing B.1: Sine Wave Reference Generator

```
1
2 clear all
3 close all
4 clc
5
6 sample = 1e-3; % sample time
7 s_des = 1; % [mm] amplitude
8 t_des = 0.1; % [s] rise time desired
9 t_start = 3; %[s] delay time
10
11 %% Design
12
13 t_interval = 0:sample:t_des;
14 syms t
15
16 f = 1/(2*t_des);
17 c = (2*s_des)/(1-cos(f*2*pi*t_des));
18 s = c * (( 1 - cos( f*2*pi*t ) ) / 2 );
19
```

```
20 S = c * (( 1 - cos( f*2*pi*t_interval ) ) / 2 );
21
22 figure
23 fplot( matlabFunction(s), [0 t_des] )
24 grid on
25
26 % add start delay
27 %wait t_start sec before starting
28 START = zeros(round(t_start/sample), 1);
29
30 TIME = 0:sample:(t_start+t_des);
31
32 X.time = TIME;
33 X.signals.values = [START; S'];
34
35 figure
36 plot(X.time,X.signals.values)
37 ylim([-0.1 1.1])
38 xlim([2.98 3.11])
39 grid on
```

Appendix C

Nonlinear Stiffness Function

Listing C.1: Stiffness Function

```
1
2 function Kx = K_function(ex,x_FDBK)
3 %#codegen
4
5     E = 69e9; % [Pa]
6
7     W_CBPM = 0.04; % [m]
8     T_CBPM = 0.001; % [m]
9     l_CBPM = 0.05; % [m]
10    Kt_CBPM = 4 * ((E * W_CBPM * T_CBPM^3) / l_CBPM^3); % [N/m]
11    EI_CBPM = E * (1/12) * W_CBPM * T_CBPM^3;
12    d = 12 / (T_CBPM / l_CBPM)^2;
13
14    W_XYZ = 0.001; % [m]
15    T_XYZ = 0.001; % [m]
16    l_XYZ = 0.05; % [m]
17    Kt_XYZ = 24 * ((E * W_XYZ * T_XYZ^3) / l_XYZ^3); % [N/m]
18
19    x_FDBK2 = x_FDBK*x_FDBK;
```

```
20 D = l_CBPM^5 / d + ((x_FDBK2*l_CBPM^3)/700);
21
22
23 if ((x_FDBK+ex) < 0)
24     error = 2.19e4;
25 else
26     error = 2.5432e4;
27 end
28
29 k = Kt_CBPM + EI_CBPM*((8.64*x_FDBK2 / D) - ...
30     ((5.76 * l_CBPM^3 * x_FDBK2*x_FDBK2)...
31     / (700 * D^2))) + Kt_XYZ + error;
32
33
34 Kx = k*ex;
```


Appendix D

Nonlinear Force Function

Listing D.1: Elastic Force Function

```
1
2 function F = delta(x)
3 %#codegen
4     E = 69e9; % [Pa]
5
6     W_CBPM = 0.04; % [m]
7     T_CBPM = 0.001; % [m]
8     l_CBPM = 0.05; % [m]
9     Kt_CBPM = 4 * ((E * W_CBPM * T_CBPM^3) / l_CBPM^3); % [N/m]
10    EI_CBPM = E * (1/12) * W_CBPM * T_CBPM^3;
11    d = 12 / (T_CBPM / l_CBPM)^2;
12
13    W_XYZ = 0.001; % [m]
14    T_XYZ = 0.001; % [m]
15    l_XYZ = 0.05; % [m]
16    Kt_XYZ = 24 * ((E * W_XYZ * T_XYZ^3) / l_XYZ^3); % [N/m]
17
18    D = l_CBPM^5 / d + ((x^2 * l_CBPM^3) / 700);
19
```

```
20     if (x < 0)
21         errorL = 2.19e4;
22         errorN = 1.18;
23     else
24         errorL = 2.5432e4;
25         errorN = 1.6;
26     end
27
28     % Theoretical Values
29     % errorL = 0;
30     % errorN = 2.88;
31
32     F = (Kt_CBPM + Kt_XYZ + errorL) * x + ...
33         (errorN * EI_CBPM * x^3) / D;
```

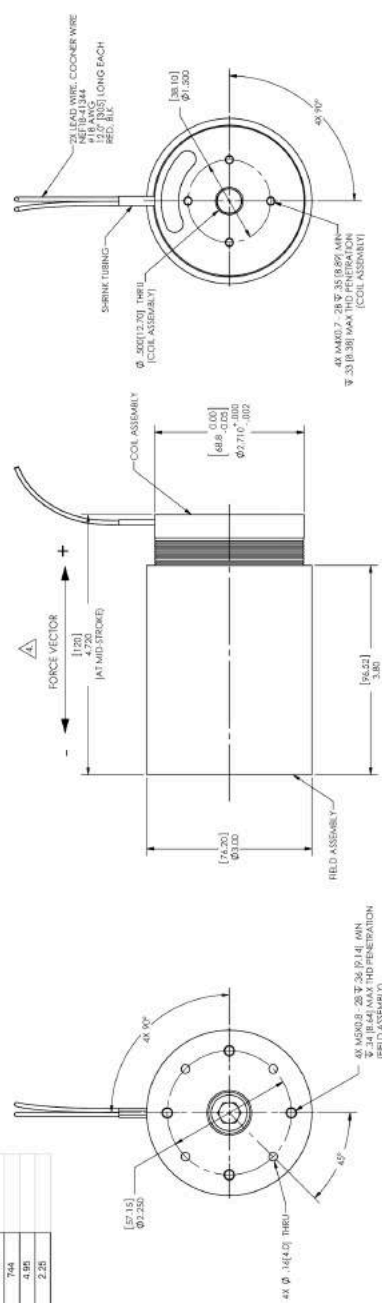
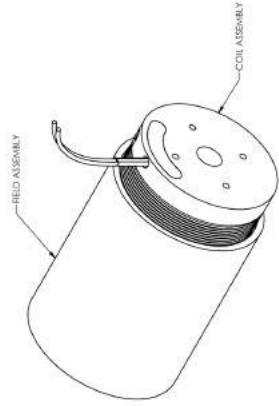
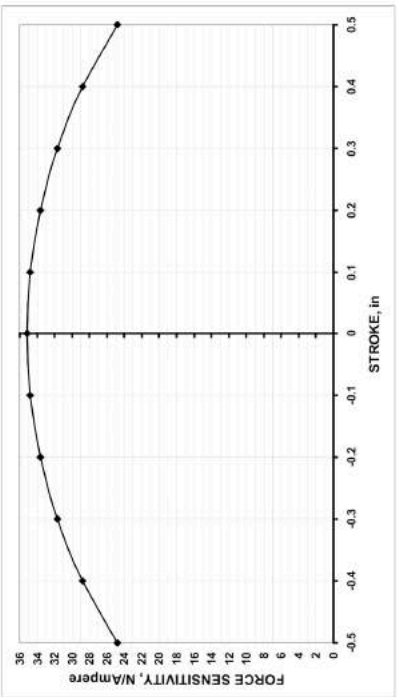
Appendix E

Datasheets

The following datasheets of the devices of the system are shown:

- Voice Coil Actuator: LA30-48-000A, BEI Technologies
- Optical Encoder: SI-HN-4000-01-0-FN-403-003-3, Ranishaw
- Controller Board: DS1104 R&D, dSPACE

REV	ECD NO.	DESCRIPTION	CHKD	APPD	DATE
X1	100134	INITIAL RELEASE	RCG	RCG	06/17/10
X2	130169	UPDATED PARAMETERS TO ASSEMBLY DRAWING	RCG	RCG	06/22/13



Winding Constants *	Units	Tol	Symbol	Wdg	A
DC Resistance	Ohms	± 12.5%	R	26	2.6
Voltage @ I _p	Volts	± 10%	V _p	33.0	3.3
Current @ I _p	Amps	± 10%	I _p	13.7	1.37
Force Sensitivity	N/Amp	± 10%	K _f	7.9	0.79
Back EMF Constant	V/(Hz)	± 10%	K _b	35.14	3.514
Inductance ***	mH-Henry	± 30%	L	35.14	3.514

Linear Actuator Parameters *	Units	Symbol	Value
Peak Force **	LB	F _p	100
Continuous Stall Force ***	LB	F _s	445
Actuator Constant	LB./V _{in}	F _s /V _s	301.1
Electrical Time Constant	ms	τ _e	133.8
Mechanical Time Constant	ms	τ _m	4.9
Theoretical Acceleration	m/sec ²	a _t	21.8
Max Theoretical Frequency @ Full Stroke & Sinusoidal Impulsive Motion	Hz	f _{max}	1.12
Power In @ I _p	Watts	P _i	1082.2
Stroke	in	S	0.9811
Clearance on Each side of Coil	mm	C	34.5384
Thermal Resistance of Coil to Still Air	°C/Watt	R _{th}	4.19
Maximum Allowable Coil Winding Temp	°C	T _{max}	0.5
Weight of Coil Assembly	LB	W _c	0.02
Weight of Field Assembly	LB	W _f	0.55
	KG	WT	2.3

* AT MID-STROKE POSITION AND @ 25°C AMBIENT TEMPERATURE
 ** MEASURED AT 1000 Hz
 *** MEASURED AT 1000 Hz



BEI KIMCO MAGNETICS DIVISION
 VISTA, CA 92081

DATE	06/14/10
DESIGNED BY	GUERRERO
DESIGNED BY	MCGHEE
DATE	06/14/10
DESIGNED BY	GOODIN
DATE	06/14/10
DESIGNED BY	GOODIN

DATE	06/14/10
DESIGNED BY	GUERRERO
DATE	06/14/10
DESIGNED BY	MCGHEE
DATE	06/14/10
DESIGNED BY	GOODIN
DATE	06/14/10
DESIGNED BY	GOODIN

LINEAR ACTUATOR

LA30-48-000A X2

THESE COMPONENTS, TECHNOLOGY OR SOFTWARE IS EXPORTED FROM THE UNITED STATES OF AMERICA IN ACCORDANCE WITH EAR AND EARLIER EDITIONS OF THE EXPORT ADMINISTRATION REGULATIONS, IN ACCORDANCE WITH U.S. LAW IS PROHIBITED.

REPRODUCTION OF THIS DOCUMENT IS PROHIBITED WITHOUT THE WRITTEN PERMISSION OF BEI KIMCO MAGNETICS DIVISION.

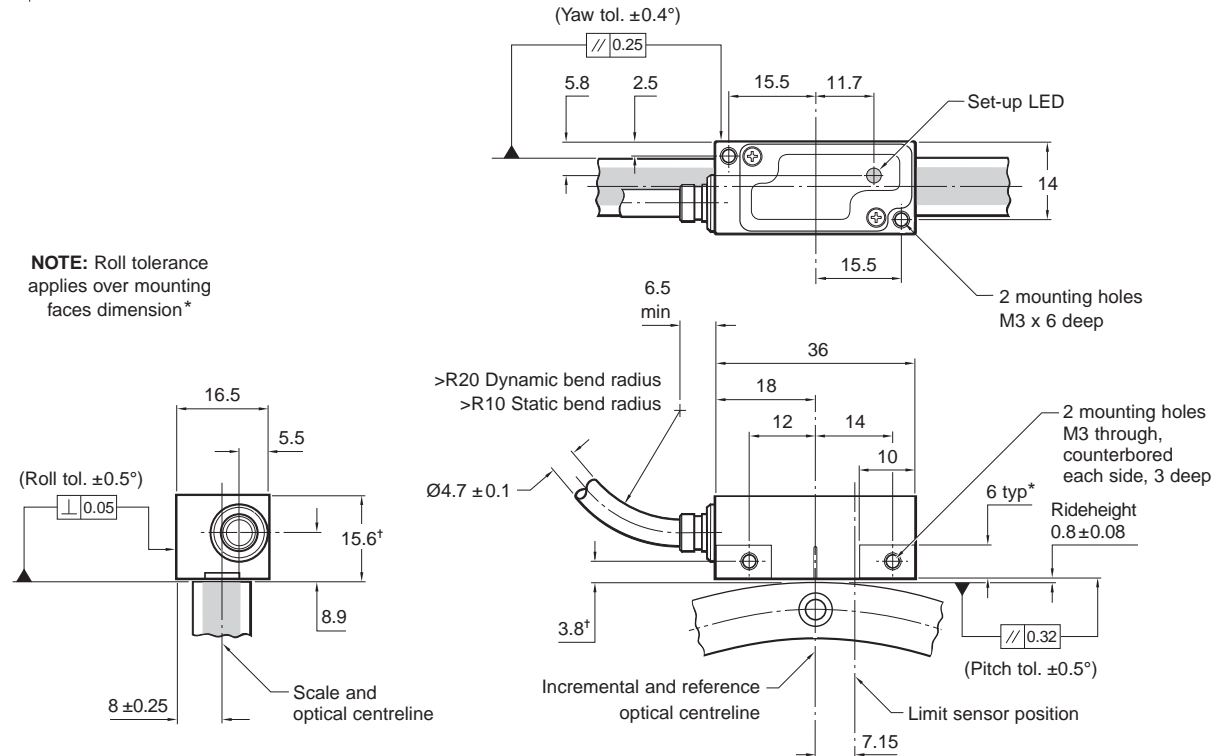
1. A POSITIVE (+) VOLTAGE APPLIED TO THE BLACK LEAD WILL PRODUCE A FORCE ON THE COIL IN THE POSITIVE (+) DIRECTION.
2. ALL DIMENSIONS ARE IN MILLIMETERS UNLESS OTHERWISE SPECIFIED.
3. ALL DIMENSIONS ARE IN MILLIMETERS UNLESS OTHERWISE SPECIFIED.
4. INTERPRET DRAWING IN ACCORDANCE WITH ISO 100.
5. INTERPRET DIMENSIONING AND TOLERANCING IN ACCORDANCE WITH ASME Y14.5M-1994.

NOTES: UNLESS OTHERWISE SPECIFIED

SR installation drawing (on RESM scale)

Dimensions and tolerances in mm

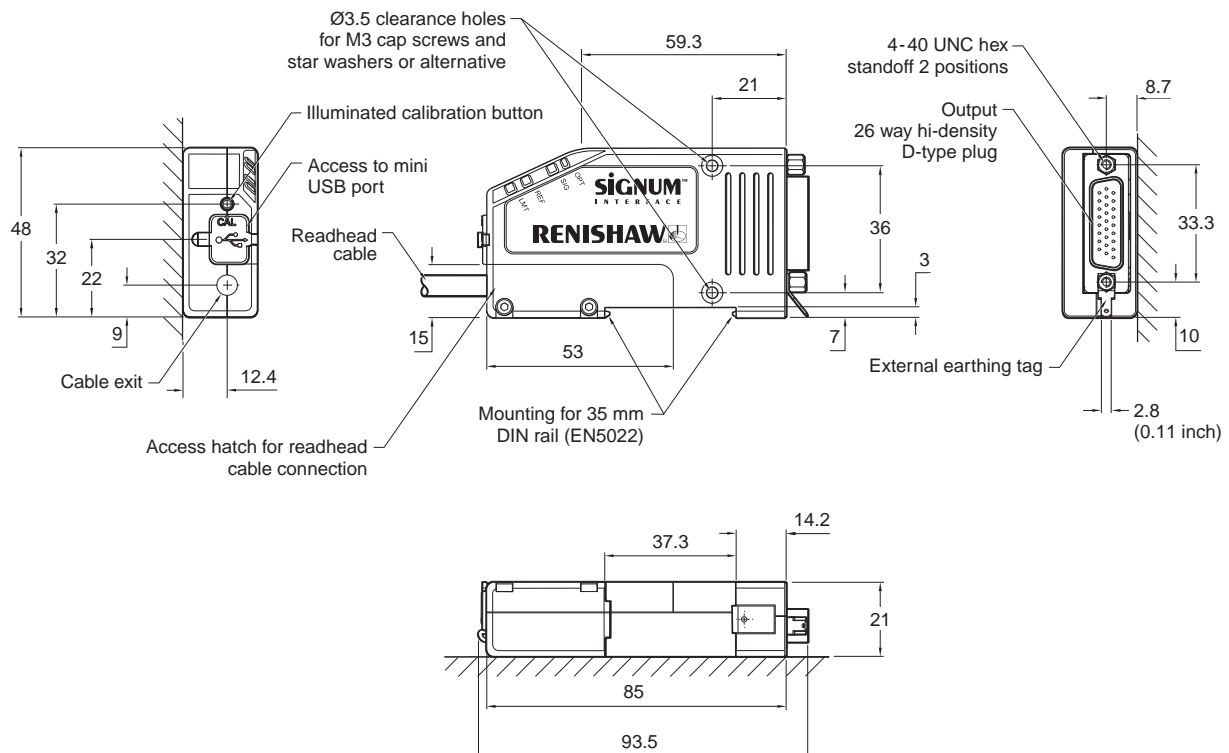
For detailed drawings, please refer to the SIGNUM linear or rotary encoder installation guides




†Dimensions from scale surface

Si installation drawing

Dimensions and tolerances in mm



Operating and electrical specifications

Power supply	5 V ±10%	<250 mA (typical)
	Ripple	200 mVpp maximum @ frequency up to 500 kHz maximum
Temperature (system)	Storage	-20 °C to +70 °C
	(readhead) Operating	0 °C to +85 °C
	(interface) Operating	0 °C to +70 °C
Humidity	Rated up to +40 °C, 95% maximum relative humidity (non-condensing)	
Sealing (readhead)		IP64
	(interface)	IP30
Acceleration (readhead)	Operating	500 m/s ² BS EN 60068-2-7:1993 (IEC 68-2-7:1983)
Shock (system)	Non-operating	1000 m/s ² , 6 ms, ½ sine BS EN 60068-2-27:1993 (IEC 68-2-27:1987)
Vibration (system)	Operating	100 m/s ² max @ 55 Hz to 2000 Hz BS EN 60068-2-6:1996 (IEC 68-2-6:1995)
Mass	Readhead	15 g
	Interface	205 g
	Cable	35 g/m
Environmental	Compliant with EU Directive 2002/95/EC (RoHS)	
EMC compliance (system)	BS EN 61326-1: 2006	
Readhead cable	Double-shielded, outside diameter 4.7 ±0.1 mm maximum Flex life >20 x 10 ⁶ cycles at 20 mm bend radius UL recognised component 	

NOTE: Class 1M LED product. LED radiation. Do not view directly with optical instruments.

Speed

Digital systems:

Minimum counter clock frequency (MHz)	Maximum speed (m/s)								
	Si-NN-0004 5 µm	Si-NN-0020 1 µm	Si-NN-0040 0.5 µm	Si-NN-0100 0.2 µm	Si-NN-0200 0.1 µm	Si-NN-0400 50 nm	Si-NN-1000 20 nm	Si-HN-2000 10 nm	Si-HN-4000 5 nm
40	12.5	12.5	12.5	5	2.5	1.25	0.5	0.27	0.135
20	12.5	12.5	6.5	2.7	1.25	0.6	0.25	0.135	0.068
12	12.5	8	4	1.5	0.8	0.4	0.15	0.09	0.045
10	12.5	6.5	3	1.25	0.6	0.3	0.12	0.068	0.034
8	12.5	5	2.5	1	0.5	0.25	0.1	0.054	0.027
6	12.5	4	2	0.8	0.4	0.2	0.08	0.045	0.023
4	12.5	3	1.5	0.6	0.3	0.15	0.06	0.034	0.017
1	4	0.8	0.4	0.15	0.075	0.04	0.02	0.008	0.004
Analogue output	12.5 m/s					3.0 m/s			

Additional decimal and binary interpolation factors are available on request

Analogue systems:

Si-NN-0000 – 12.5 m/s Si-NN-0001 (bandwidth limited for lower noise) – 3.0 m/s

Angular speed depends on ring diameter - use the following equation to convert to rev/min

$$\text{Angular speed (rev/min)} = \frac{V \times 1000 \times 60}{\pi D} \quad \text{Where } V = \text{maximum linear speed (m/s) and } D = \text{external diameter of RESM (mm)}$$

Output specifications

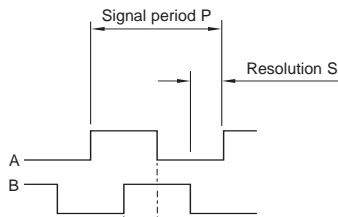
Digital output signals - available from all Si interfaces
except Si-NN-0000 and Si-NN-0001

All digital SiGNUM interfaces also offer analogue outputs as standard

Form - Square wave differential line driver to EIA RS422A
(except limits P and Q and warning W)

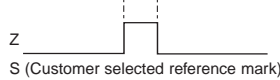
Analogue output signals - available from all
Si interfaces

Incremental 2 channels A and B in quadrature
(90° phase shifted)[†]



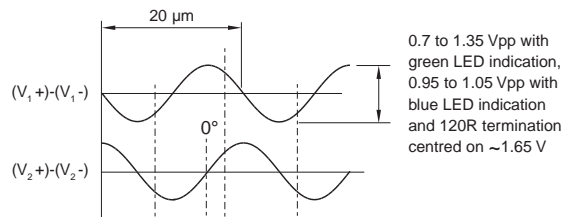
Model	P (µm)	S (µm)
Si-NN-0004	20	5
Si-NN-0020	4	1
Si-NN-0040	2	0.5
Si-NN-0100	0.8	0.2
Si-NN-0200	0.4	0.1
Si-NN-0400	0.2	0.05
Si-NN-1000	0.08	0.02
Si-HN-2000	0.04	0.01
Si-HN-4000	0.02	0.005

Reference[†]



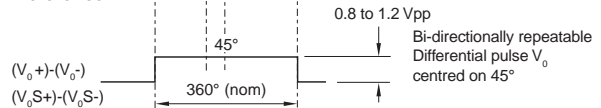
Bi-directionally repeatable pulse Z,
with duration equal to the resolution

Incremental 2 channels V_1 and V_2 differential sinusoids in quadrature
(90° phase shifted)[†]



0.7 to 1.35 Vpp with
green LED indication,
0.95 to 1.05 Vpp with
blue LED indication
and 120R termination
centred on ~1.65 V

Reference[†]



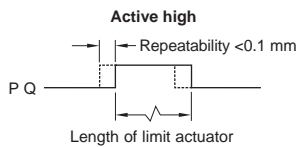
0.8 to 1.2 Vpp
Bi-directionally repeatable
Differential pulse V_0
centred on 45°

All units

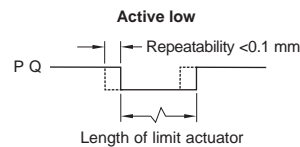
End of travel limit and warning outputs can be selected as 'active high' or 'active low' at time of ordering.

The alarm signal can be output as a differential line driven signal or 3-state. Again, please select the preferred option at time of ordering.

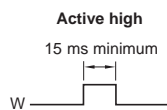
Limits Open collector output, asynchronous pulse



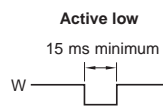
or



Warning Open collector output, asynchronous pulse

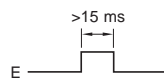


or



Warning asserted when $50\% > V_1/V_2 > 130\%$.
Other warning triggers available on request,
please contact your Renishaw representative
for further details.

Alarm[†] Asynchronous pulse



Alarm asserted when signal level is less than 20% or
greater than 135% and overspeed. Alarm is also asserted
if readhead speed is too high for reliable operation.
Other alarm triggers available on request, please contact
your Renishaw representative for further details.

or 3-state alarm

Differentially transmitted signals forced open circuit
for >15 ms when alarm conditions valid.

[†]Inverse signals not shown for clarity

Technical Details

Parameter		Specification
Processor		<ul style="list-style-type: none"> ■ MPC8240 processor with PPC 603e core and on-chip peripherals ■ 64-bit floating-point processor ■ CPU clock: 250 MHz ■ 2 x 16 KB cache, on-chip
Memory	Global memory	■ 32 MB SDRAM
	Flash memory	■ 8 MB
Timer	4 general-purpose timers	<ul style="list-style-type: none"> ■ 32-bit down counter ■ Reload by hardware ■ 80-ns resolution
	1 sampling rate timer (decrementer)	<ul style="list-style-type: none"> ■ 32-bit down counter ■ Reload by software ■ 40-ns resolution
	1 time base counter	<ul style="list-style-type: none"> ■ 64-bit up counter ■ 40-ns resolution
Interrupt controller		<ul style="list-style-type: none"> ■ 5 timer interrupts ■ 2 incremental encoder index line interrupts ■ 1 UART interrupt ■ 1 slave DSP interrupt ■ 1 slave DSP PWM interrupt ■ 5 A/D converter (end of conversion) interrupts ■ 1 host interrupt ■ 4 external interrupts (user interrupts)
A/D converter	Channels	<ul style="list-style-type: none"> ■ 4 multiplexed channels equipped with one sample & hold A/D converter (1x16-bit) ■ 4 parallel channels each equipped with one sample & hold A/D converter (4x12-bit) ■ Note: 5 A/D converter channels (1x16-bit and 4x12-bit) can be sampled simultaneously
	Resolution	<ul style="list-style-type: none"> ■ Multiplexed channels: 16 bit ■ Parallel channels: 12 bit
	Input voltage range	■ ±10 V
	Conversion time	<ul style="list-style-type: none"> ■ Multiplexed channels: 2 μs¹⁾ ■ Parallel channels: 800 ns¹⁾
	Offset error	■ ±5 mV
	Gain error	<ul style="list-style-type: none"> ■ Multiplexed channels: ±0.25% ■ Parallel channels: ±0.5%
	Offset drift	■ 40 μV/K
	Gain drift	■ 25 ppm/K
	Signal-to-noise ratio	<ul style="list-style-type: none"> ■ Multiplexed channels: >80 dB ■ Parallel channels: >65 dB
D/A converter	Channels	■ 8 channels
	Resolution	■ 16-bit
	Output range	■ ±10 V
	Settling time	■ Max. 10 μs (full-scale, accuracy ½ LSB)
	Offset error	■ ±1 mV
	Gain error	■ ±0.1%
	Offset drift	■ 130 μV/K
	Gain drift	■ 25 ppm/K
	Signal-to-noise ratio	■ >80 dB
	I _{max}	■ ±5 mA
Digital I/O	Channels	<ul style="list-style-type: none"> ■ 20-bit parallel I/O ■ Single bit selectable for input or output
	Voltage range	■ TTL input/output levels
	I _{out, max}	■ ±5 mA

¹⁾ Speed and timing specifications describe the capabilities of the hardware components and circuits of our products. Depending on the software complexity, the attainable overall performance figures can deviate significantly from the hardware specifications.

Parameter		Specification	
Digital incremental encoder interface	Channels	<ul style="list-style-type: none"> 2 independent channels Selectable single-ended (TTL) or differential (RS422) input (software programmable for each channel) 	
	Position counters	<ul style="list-style-type: none"> 24-bit resolution Max. 1.65 MHz input frequency, i.e., fourfold pulse count up to 6.6 MHz Counter reset or reload via software 	
	Sensor supply voltage	<ul style="list-style-type: none"> 5 V/0.5 A 	
Serial interface	Configuration	<ul style="list-style-type: none"> Single UART (universal asynchronous receiver and transmitter) with FIFO PLL-driven UART for accurate baud rate selection RS232/RS422/RS485 compatibility 	
	Baud rate	<ul style="list-style-type: none"> Up to 115.2 kBd (RS232) Up to 1 MBd (RS422/RS485) 	
Slave DSP	Type	<ul style="list-style-type: none"> Texas Instruments TMS320F240 DSP 16-bit fixed-point processor 	
	Clock rate	<ul style="list-style-type: none"> 20 MHz 	
	Memory	<ul style="list-style-type: none"> 64Kx16 external code memory 28Kx16 external data memory 4Kx16 dual-port memory for communication 32 KB flash memory 	
	I/O channels ¹⁾	<ul style="list-style-type: none"> 10 PWM outputs 4 capture inputs 1 serial peripheral interface 	
	Input voltage range	<ul style="list-style-type: none"> TTL input/output level A/D converter inputs: 0 ... 5 V 	
	Output current	<ul style="list-style-type: none"> Max. ±13 mA 	
Host interface (requires one PCI or one PCIe x 1 slot)		PCI	PCIe
Physical characteristics	Physical size	<ul style="list-style-type: none"> 185 x 107 mm (7.28 x 4.2 in) 	<ul style="list-style-type: none"> 220 x 111 mm (8.66 x 4.3 in)
	Ambient temperature	<ul style="list-style-type: none"> 0 ... 55 °C (32 ... 131 °F) 	<ul style="list-style-type: none"> 0 ... 55 °C (32 ... 131 °F)
	Cooling	<ul style="list-style-type: none"> Active cooling by fan 	<ul style="list-style-type: none"> Active cooling by fan
	Power consumption	<ul style="list-style-type: none"> 18.5 W 	Please inquire
	Power supply	<ul style="list-style-type: none"> +5 V ±5%, 2.5 A +12 V ±5%, 0.3 A -12 V ±5%, 0.2 A 	Please inquire

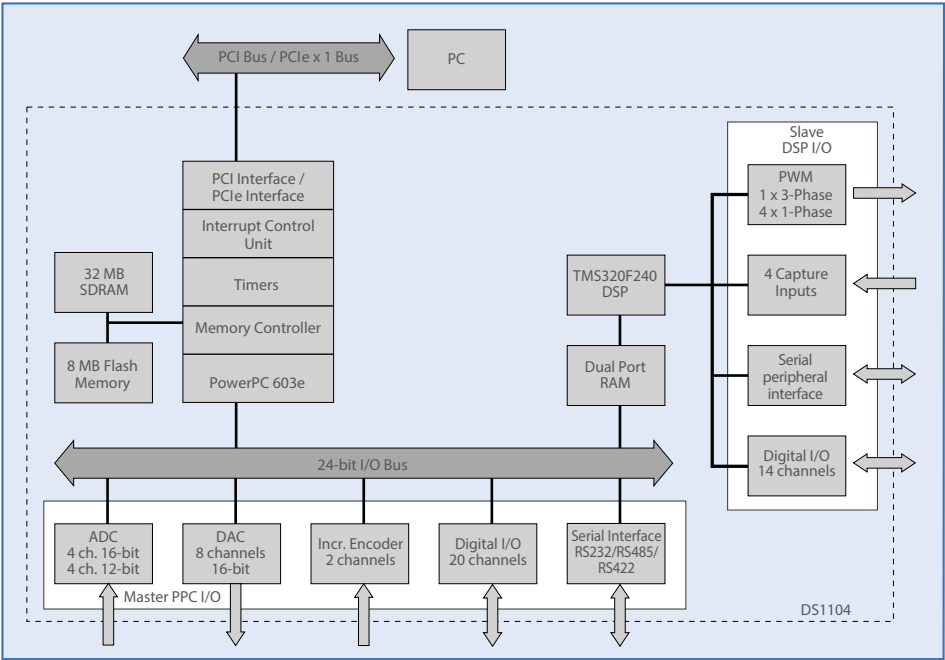
¹⁾ The exact number of I/O channels depends on your configuration and is described in the user documentation.

Connector Panels

All I/O signals of the DS1104 R&D Controller Board can usually be accessed via adapter cables. A more convenient solution is I/O access via connector panels, which make the signals available in either a 19" rack or a 19" desktop box. The panels are tailored to a specific controller board, so that you have all the signals for easy connection to the real world at your disposal.

- Connector Panels (p. 328)

Block Diagram



References

- [1] Alex Owen-Hill, “*How to Calculate a Robot’s Forward Kinematics in 5 Easy Steps.*” <https://blog.robotiq.com/how-to-calculate-a-robots-forward-kinematics-in-5-easy-steps>, November 2015
Serial Robot image.
- [2] Stefan Staicu, “*Dynamic Analysis of Clavel’s Delta Parallel Robot.*” <https://www.semanticscholar.org/paper/Dynamic-analysis-of-Clavel’s-delta-parallel-robot-Staicu-Carp-Ciocardia/db734650297673987b99f3462a28b673f6c3b565>, 2003
Parallel Robot image.
- [3] Guangbo Hao, “*Advanced Robotics,*” ME6012 Class Notes, University College Cork, 2018
Compliant Mechanisms.
- [4] BYU-CMR, “*Compliant Mechanisms Explained.*” <https://www.compliantmechanisms.byu.edu/about-compliant-mechanisms>,
Compliant mechanism images.
- [5] Haiyang Li, “*Approaches to the Synthesis, Modelling and Optimisation of Spatial Translational Compliant Parallel Mechanisms,*” PhD Thesis, University College Cork, Ireland, November 2016
Thesis about the design of the XYZ CPM.

- [6] Guangbo Hao and Haiyang Li, “*Extended Static Modeling and Analysis of Compliant Compound Parallelogram Mechanisms Considering the Initial Internal Axial Force*,” ASME IDETC2015 conference, Boston, 2015; Journal of Mechanisms and Robotics, Mar 07, 2016
Paper for Nonlinear model design of CBPMs.
- [7] Riccardo Sandon, “*Modelling, Control and Performance Evaluation of a Single-Axis Compliant Nano-Positioning System*,” Master thesis, University of Padua, 2017
Master thesis [same project], detailed "startup condition".
- [8] Haiyang Li, Guangbo Hao and Richard Kavanagh, “*A New XYZ Compliant Parallel Mechanism for Micro/Nano-Manipulation: Design and Analysis*,” University College Cork, Cork, Ireland; Micromachines, Feb 1, 2016
Paper about the design of the XYZ CPM.
- [9] Danielle Collins, “*How do rotary voice coil actuators work?*”
<https://www.motioncontroltips.com/how-do-rotary-voice-coil-actuators-work/>,
Motion Control Tips, July 2018
Introduction to Voice Coil Actuators.
- [10] Neal Gordon, “*Mechanical Vibrations with Python*.”
<http://ifcuriousthenlearn.com/blog/2015/06/09/mechanical-vibrations-with-python/>, June 2015
Mass-Spring-Damper system image.
- [11] Guangbo Hao and Haiyang Li, “*Nonlinear Analytical Modeling and Characteristic Analysis of a Class of Compound Multi-beam Parallelogram Mechanisms*,” Journal of Mechanisms and Robotics, Nov 01, 2015
Paper for Nonlinear model design of CBPMs.

- [12] Ram Dušić Hren, “*Nonlinear Oscillators*,” Seminar Ia - I. year of Bologna II. cycle
Introduction Nonlinear Duffing Oscillator.
- [13] A.B. Barrett, “*The Application of Observers in Position Servosystems*,” M. Eng. Sc. thesis, National University of Ireland, June 1992
Discrete Observer Analysis.
- [14] Wikipedia, “*PID Controller*.”
https://en.wikipedia.org/wiki/PID_controller,
PID Controller Basics.
- [15] ISO 5725-1, “*Accuracy (trueness and precision) of measurement methods and results-Part 1: General principles and Definitions*,” 1994
Definition of Accuracy and Precision.
- [16] Brigham Young University - BYU, “*Intro to Compliant Mechanisms*.”
<https://compliantmechanisms.byu.edu/content/intro-compliant-mechanisms>, Compliant Mechanisms Research
Introduction to Compliant Mechanisms.
- [17] Douglass L. Blanding, “*Principles of Exact Constraint Mechanical Design*,” Eastman Kodak Company, 1992
Exact Constraint Design Definition for Compliant Mechanism.
- [18] Fabiana Federica Ferro, “*Nonlinear Control of a Flexure-Based Single Degree of Freedom Nanopositioning System*,” Master thesis, University of Padua, 2016
Master thesis [same project] with useful setup guidelines.
- [19] Riccardo Sandon, Richard Kavanagh and Guangbo Hao, “*High-Performance Control of a Single-Axis Compliant Nano-Positioning System: Design*,” 34th Intl. Manufacturing Conf, Aug 30-31, 2017
Paper on the same project.

- [20] Shorya Awtar, “*Synthesis and Analysis of Parallel Kinematic XY Flexure Mechanisms*,” Sc.D. thesis, Indian Institute of Technology, Kanpur (India), 1998
Thesis about the evaluation of nonlinear load-displacement equations for CBPMs.
- [21] A.K. Mallik, “*Response of A Hard Duffing Oscillator to Harmonic Excitation – An Overview*,” Indian Institute of Technology, Kanpur (India), Dec 28-30, 2003
Response of a Duffing oscillator to harmonic excitation.
- [22] Kim Doang Nguyen, I-Ming Chen and Teck-Chew Ng, “*Planning Algorithms for S-curve Trajectories*,” IEEE, Singapore, October 2007
S-Curve in motion control.
- [23] Robert D. Lorenz and Douglas J. Sykora, “*A Direct-Drive, Robot Parts, and Tooling Gripper with High-Performance Force Feedback Control*,” IEEE Transactions on Industry Applications vol. 27 no.2, March/April 1991
Paper with Force Feedforward design guidelines.
- [24] Richard Kavanagh, “*Industrial Automation and Control*,” EE4014 Class Notes, University College Cork, 2018
Observer description.
- [25] Lennart Ljung, “*Lennart Ljung on System Identification Toolbox*.”
<https://uk.mathworks.com/videos/series/lennart-ljung-on-system-identification-toolbox-97005.html>,
MathWorks
Tutorial and history of System Identification Toolbox.
- [26] Guangbo Hao, Xianwen Kong and Robert L. Reuben, “*A Nonlinear Analysis of Spatial Compliant Parallel Modules: Multi-Beam Modules*,”

Heriot-Watt University, Edinburgh, UK, March 2011

Four-beam compliant module reaction forces analysis.

- [27] Riccardo Sandon, Guangbo Hao and Richard Kavanagh, “*High-Performance Control of a Single-Axis Compliant Nano-Positioning System: Control*,” 34th Intl. Manufacturing Conf, Aug 30-31, 2017

Paper on the same project.